

REPORT DOCUMENTATION PAGE

Form Approved
OMB NO. 0704-0188

Public reporting burden for this collection of information is estimated to average 1 hour per response, including the time for reviewing instructions, searching existing data sources, gathering and maintaining the data needed, and completing and reviewing the collection of information. Send comment regarding this burden estimate or any other aspect of this collection of information, including suggestions for reducing this burden, to Washington Headquarters Services, Directorate for Information Operations and Reports, 1215 Jefferson Davis Highway, Suite 1204, Arlington, VA 22202-4302, and to the Office of Management and Budget, Paperwork Reduction Project (0704-0188), Washington, DC 20503.

1. AGENCY USE ONLY (Leave blank)		2. REPORT DATE	3. REPORT TYPE AND DATES COVERED FINAL 15 Sep 94 - 14 Sep 99	
4. TITLE AND SUBTITLE Engine Research Center: Advanced Diesel Engine Research			5. FUNDING NUMBERS DAAH04-94-G-0328	
6. AUTHOR(S) Professors: M. Corradini, P. Farrell, D. Foster, J. Ghandhi, J. Martin, R. Reitz, C. Rutland				
7. PERFORMING ORGANIZATION NAME(S) AND ADDRESS(ES) University of Wisconsin-Madison			8. PERFORMING ORGANIZATION REPORT NUMBER	
9. SPONSORING / MONITORING AGENCY NAME(S) AND ADDRESS(ES) U.S. Army Research Office P.O. Box 12211 Research Triangle Park, NC 27709-2211			10. SPONSORING / MONITORING AGENCY REPORT NUMBER ARO 33804.11-EG	
11. SUPPLEMENTARY NOTES The views, opinions and/or findings contained in this report are those of the author(s) and should not be construed as an official Department of the Army position, policy or decision, unless so designated by other documentation.				
12a. DISTRIBUTION / AVAILABILITY STATEMENT Approved for public release; distribution unlimited.				
13. ABSTRACT (Maximum 200 words) The objectives of the Engine Research Center (ERC) are to conduct research leading to improved diesel engines, to provide trained manpower for U.S. needs, and to cooperate in technical information exchange with Army and other engine laboratories. Fundamental projects addressing continued development of advanced multidimensional modeling, advanced diagnostic development, experimental investigation of fluid mechanic mixing phenomena and engine experiments aimed at understanding the potential for increased power density were undertaken. The attached report is divided into four sections. Each section concludes with a list of relevant references. The first section reports the results of computational methodology efforts. The projects summarized include engine optimization via computational algorithms. The second section summarizes the research on fluid mixing layers and diagnostics development, which highlights the fundamental work on non-premixed reacting shear layers and the investigation of laser fluorescence of CH as a flame front marker. The third section gives a detailed account of the work pursuing the potential for increased power density through enhanced in-cylinder mixing. The final section is a detailed report on the effect of intake air or fuel composition manipulation on engine performance relative to its potential to increase power density without increasing smoke.				
14. SUBJECT TERMS Internal Combustion Engine, Power Density, Diagnostic Development, Fluid Mechanic Modeling, KIVA 3D Modeling			15. NUMBER OF PAGES 71	
			16. PRICE CODE	
17. SECURITY CLASSIFICATION OR REPORT UNCLASSIFIED	18. SECURITY CLASSIFICATION OF THIS PAGE UNCLASSIFIED	19. SECURITY CLASSIFICATION OF ABSTRACT UNCLASSIFIED	20. LIMITATION OF ABSTRACT UL	

Table of Contents

	Page
List of manuscripts published	2
Personnel supported, degrees awarded and theses published (Under ARO Sponsorship)	3
Personnel supported who have not yet received degrees	5
Statement of Problem Studied	5
Summary of Research Findings	5
Computational Methodology for Engine Design	5
Optimization of Diesel Engine Operating Parameters Using Design of Experiments	6
Multi-dimensional Simulation of Diesel Engine Cold Start	7
Comparison of Predicted Diesel Spray Liquid Penetration with Optical Measurements	8
Modeling the Effect of Premixed Combustion on Diesel Engine NO _x	10
References for Computational Methodology for Engine Design	11
Planar Reacting Shear Layer	11
Calibration of the Laser-Induced Fluorescence Technique for Measuring Oil Film Thickness at the Ring Reversal Region of a SI Engine by Using Capacitance Gauges	14
Demonstration of a Diagonal Excitation/Observation Technique for Laser Induced Fluorescence of the CH Radical in Atmospheric Pressure Flames	14
References for Diagonal Excitation/Observation research	23
Parameters That Affect the Impact of Auxiliary Gas Injection in a DI Diesel Engine	24
References for Auxiliary Gas Injection research	39
Effects of Oxygen Enhancement on the Emission from a DI Diesel via Manipulation of Fuels and Combustion Chamber Gas Composition	40
References for Oxygen Enhancement research	69
Report of Inventions	71

TECHNICAL FINAL REPORT

1. ARO Proposal Number 30340-EG-URI

2. Period Covered by the Report: 16 September 1994 - 15 September 1999

3. Title of Proposal: URI Multidisciplinary Research Program for FY92-FY96 on Engine Combustion (No cost extension until 31 December 1997) Engine Research Center: Advanced Diesel Engine Research

4. Contract or Grant Number: DAAH04-94-G-0328

5. Name of Institution: University of Wisconsin - Madison

6. Authors of the Report: Professors: M. Corradini, P. Farrell, D. Foster, J. Ghandhi, J. Martin, R. Reitz, C. Rutland

7. Manuscripts published (and accepted for publication) under ARO Sponsorship

C.J. Rutland, N. Ayoub, Z.Han, G.Hampson, S.-C.Kong, K. Mather, D. Montgomery, M. Musculus, M. Patterson, D. Pierpoint, L. Ricart, P.Stephenson, and R.D. Reitz, "Diesel Engine Model Development and Experiments," 1995. SAE 951200, 1995 SAE Earth Moving Conference, April 4-5, Peoria, IL.

M. Al-Roub and P.V Farrell, "Droplet-Wall Impingement for Multiple Droplet Events," accepted for ASME Internal Combustion Engines Meeting, April 1995

T.F. Su, K. Goney, D. Schmidt, M. Corradini, and P.V. Farrell, "Cavitation in Diesel Fuel Injectors," submitted for 8th International Symposium on Multiphase Flow in Combustion, San Francisco, July 1995

David P. Schmidt, Tzay-Fa Su, Kayhan H. Goney, P.V. Farrell and M.L. Corradini. "Detection of Cavitation in Fuel Injector Nozzles." 8th ISTP Conference, San Francisco, July 1995.

C.Y Choi, D.E. Foster, "In Cylinder Augmented Mixing Through Controlled Gaseous Jet Injection," SAE 952358

Nabil S. Ayoub, Rolf D. Reitz, "Multidimensional Modeling of Fuel Composition Effects on Combustion and Cold-Starting in Diesel Engines," SAE 95245

C.J. Rutland, N. Ayoub, Z. Han, G. Hampson, S.-C. Kong, D. Mather, M. Musculus, M. Patterson, L. Ricart, P. Stephenson, R.D. Reitz, "Progress Towards Diesel Combustion Modeling," SAE 952429

M. Al-Roub, J. Senda, and P.V. Farrell, "New-Wall Interaction in Spray Impingement", SAE Paper 960863

N.S. Ayoub, and R.D. Reitz, "Multidimensional Modeling of Fuel Composition Effects and Split Injections on Diesel Engine Cold-Starting." Accepted for publication. AIAA Journal of Propulsion and Power, 1996

A.S. McLandress, R.G. Emerson, P.McDowell and C.J. Rutland, "Intake and In-Cylinder Flow Modeling Characterization of Mixing and Comparison with Flow Bench Results," SAE 960635, 1996 SAE International Congress, Feb 26-29

L.M. Ricart, and R.D. Reitz, "Visualization and Modeling of Pilot Injection and Combustion in Diesel Engines," SAE 960833, 1996

Ricart, L.M., and Reitz, R.D., "Visualization and Modeling of Pilot Injection and Combustion in Diesel Engines," SAE Paper 960833, SAE Transactions, Vol. 105, Section 3, Journal of Engines, pp. 1164-1183, 1996.

Su, T., Warrick, C. and Farrell, P., "Temperature Effects On High Pressure Sprays", SAE 962005, 1996.

Ayoub, N.S., and Reitz, R.D., "Multidimensional Modeling of Fuel Composition Effects and Split Injections on Diesel Engine Cold-starting," AIAA Journal of Propulsion and Power, Vol. 13, pp. 123-130, 1997.

Senecal, P.K., Xin, J., and Reitz, R.D., "Predictions of Residual Gas Fraction in IC Engines," SAE Paper 962052, SAE Transactions, Vol. 105, Section 3, Journal of Engines, pp. 2243-2254, 1996.

Choi, C., Bower, G., and Reitz, R.D., "Effects of Biodiesel Blended Fuels and Multiple Injections on DI Diesel Engine Emissions, SAE Paper 970218, Accepted for SAE Transactions, 1997.

Ricart, L.M., Xin, J., Bower, G.R., and Reitz, R.D., "In-Cylinder Measurement and Modeling of Liquid Fuel Spray Penetration in a Heavy-Duty Diesel Engine," SAE Paper 971591, Submitted for SAE Transactions, 1997.

Senecal, P.K., Uludogan, A., and Reitz, R.D., "Development of Novel Direct-Injection Diesel Engine Combustion Chamber Designs using Computational Fluid Dynamics", SAE Paper 971594, Submitted for SAE Transactions, 1997.

Al-Roub and Farrell, P., "Atomization of Thin Liquid Films by Droplet Impact", Atomization and Sprays 7, p. 531, 1997.

Mislevy, S. and Farrell, P., "Wall Impingement Spray Characteristics", ICLASS '97, August 1997

Stanton, D.W., Senecal, P.K., Hung, C.C., Rutland, C.J., Reitz, R.D., "Methodology for Model Discrimination and Criticism for Liquid Atomization Data," Accepted for publication, Atomization and Sprays, 1998.

Xin, J., Ricart, L., and Reitz, R.D., "Computer Modeling of Diesel Spray Atomization and Combustion," Accepted for publication, Combustion Science and Technology, 1997.

Mislevy, S. and Farrell, P., "Spray Characteristics of a Diesel Fuel Spray Impinging on a Raised Surface", ILASS-Europe, July 1998

Al-Roub, M. and Farrell, P., "Heat Transfer for Impinging Drops", submitted to Journal of Heat Transfer

8a. Degrees Awarded and Theses Published (under ARO Sponsorship)

1995

Ayoub, Nabil, PhD

Modeling Multicomponent Fuel Sprays In Engines With Application To Diesel Cold-Starting

Boucher, Stephen E., MS

Preliminary Study Of A Shear Plane Layer Formed Between Two Parallel Flows.

Choi, Cathy, MS

In Cylinder Augmented Mixing Through Controlled Gaseous Jet Injection

Claybaker, Peter, MS
Streamlined Production Of Engine Meshes For Kiva-3

Krause, Steven F., MS
The Effect Of Intake Port Geometry On In-Cylinder Fluid Motion In A Reciprocating I.C. Engine.

Lee, Laurence, MS
Oil Film Thickness Between Top Piston Ring And Engine Liner Near Ring Reversal Of A Single Cylinder S.I. Engine.

McLandress, Andrew, MS
Intake Flow Mixing And Characterization For Diesel Simulations

Mehri, Darius, MS
The Design Of A High Pressure, High Temperature Turbulent Mixing Layer Apparatus

Ricart, Laura M., MS
The Effects Of Heat Transfer And Mixing On Diesel Ignition And Combustion

Stanton, Donald W., MS
Modeling Fuel Film Formation And Wall Interaction In Diesel Engines.

1996

Al-Roub, Marwan Abu, Phd
Hydrodynamics And Heat Transfer Of Multiple Droplet Impingement

Ducu, Dan O., PhD
Calibration Of The Laser Induced Fluorescence Technique Applied To Oil Film Thickness Measurements On A Diesel Engine Cylinder Liner By Using Capacitance Gauges

Emerson, Roy, MS
Intake Flow Modeling In KIVA-3 And Comparison With Experiments

Pardyjak, Eric R., MS
Development And Evaluation Of Turbulent Mixing Models

Raney, Helen E., MS
Analyzing Cycle To Cycle Variations In The Intake Flow Using A Water Analog Engine

1997

Senecal, Peter Kelly, MS
Exploring Alternatives to Conventional Di Diesel Combustion Systems Using Computational Fluid Dynamics

Schmidt, David P., Ph.D.
Cavitation in Diesel Fuel Injector Nozzles

Donahue, Richard PhD
Experimental Studies on Ring Pack Design Parameters and The Analysis of Radial Ring Collapse.

1998

Ricart, Laura, PhD

An Experimental and Computational Study of Fuel Injection, Mixing and Combustion in Diesel Engines

.....

PEOPLE WHO HAVE BEEN SUPPORTED ON THE GRANT BUT WHO HAVE NOT YET COMPLETED THESIS:

Calvin Hung, Kevin Sholes, Todd Rose, Scott Mislevy, Taewoong Hwang, Robert Borthwick, Yoshi Ieda, Robert Vets (Terminated)

STATEMENT OF THE PROBLEM STUDIED

The objectives of the Engine Research Center (ERC) are to conduct research leading to improved diesel engines, to provide trained manpower for U.S. needs, and to cooperate in technical information exchange with Army and other engine laboratories. Fundamental projects addressing continued development of advanced multidimensional modeling, advanced diagnostic development, experimental investigation of fluid mechanic mixing phenomena and engine experiments aimed at understanding the potential for increased power density were undertaken. The report below is divided into four sections. Each section concludes with a list of relevant references. The first section reports the results of computational methodology efforts. The second section summarizes the research on fluid mixing layers and diagnostics development. The third section gives a detailed account of the work pursuing the potential for increased power density through enhanced in-cylinder mixing. And the final section is a detailed report on the effect of intake air or fuel composition manipulation on engine performance.

SUMMARY OF RESEARCH FINDINGS

Computational Methodology for Engine Design

The goal of this project was to explore methods to incorporate the use of multidimensional modeling in the engine design process. Traditionally, engine design has been done using experimental trial and error and experience, coupled with cycle analysis. However, new tools such as comprehensive computer models are now available. This project aims to develop a methodology for engine combustion chamber design by using advanced computer models guided by informative experiments.

The methodology used the ERC KIVA-GA computer code, and a computational optimization study was performed for a heavy-duty direct-injection diesel engine. KIVA-GA performs full cycle engine simulations within the framework of a Genetic Algorithm (GA) global optimization code. Design fitness is determined using a one-dimensional gas-dynamics code for calculation of the gas exchange process, and a three-dimensional CFD code based on KIVA-3V for spray, combustion and emissions formation [1].

Although multi-dimensional CFD modeling provides a tool for simulating both conventional and unconventional engine design concepts, an efficient design process must be based on a mathematical or statistical scheme which "searches" a constraint-limited objective function surface for an optimum. In the present study, the CFD model was used as a function evaluator which calculates the objective function $f(\mathbf{X})$

to be optimized, where \mathbf{X} is the vector of parameters, or control factors, to be varied. In the present study, $f(\mathbf{X}) = 1000 / (R_1^2 + R_2^2 + R_3)$ where $R_1 = (\text{NOx} + \text{HC}) / W_1(\text{NOx} + \text{HC})_m$, $R_2 = \text{PM} / W_2 \text{PM}_m$, and $R_3 = \text{BSFC} / \text{BSFC}_0$ where $(\text{NOx} + \text{HC})_m$ and PM_m are 2004 EPA mandated emissions levels (3.35 and 0.13 g/kW-hr, respectively) and BSFC_0 is the baseline fuel consumption (215 g/kW-hr). W_1 and W_2 are weighting constants (safety factors) set to 0.8 for this study.

The KIVA-GA methodology was used to simultaneously investigate the effects of six engine input parameters on emissions and performance for a high speed, medium load operating point for which baseline engine experimental data was available. Start of injection (SOI), injection pressure, amount of exhaust gas recirculation (EGR), boost pressure and split injection rate-shape were explored. The predicted optimum results in significantly lower soot and NOx emissions, together with improved fuel consumption compared to the baseline design, as shown in Fig. 1. The present results indicate that an efficient computational design methodology has been developed for optimization of internal combustion engines with respect to a large number of parameters. More details are given by Senecal et al. [1, 2].

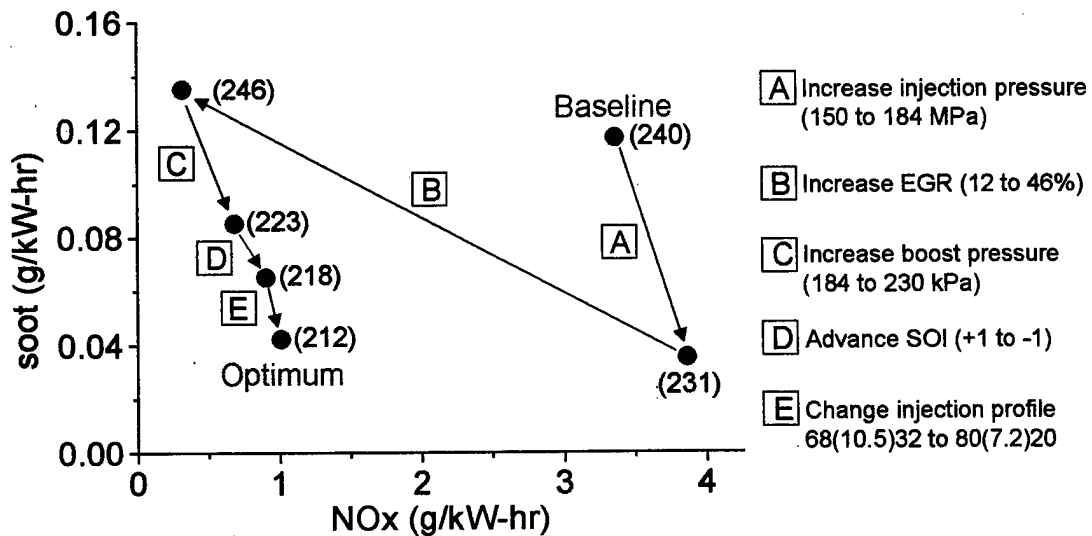


Figure 1 Predicted optimum soot and NOx for a heavy-duty diesel engine. The Baseline corresponds to the initial design and the labeled points show the individual effect of each variable in the optimization predicted by the ERC KIVA-GA methodology.

Optimization of Diesel Engine Operating Parameters Using Design of Experiments

A study of statistical methods for the optimization of engine operating parameters was conducted. The objective of the study was to develop a strategy to efficiently optimize operating parameters of diesel

engines with multiple injection and EGR capabilities. Previous studies have indicated that multiple injections with EGR can provide substantial simultaneous reductions in emissions of particulate and NO_x from heavy-duty diesel engines, but careful optimization of the operating parameters is necessary in order to receive the full benefit of these combustion control techniques [3]. The goal of the present study was to optimize the control parameters to reduce emissions and brake specific fuel consumption. An instrumented single-cylinder heavy-duty diesel engine was used with a prototype mechanically actuated (cam driven) fuel injection system [4]. Two injection systems were used, the standard Caterpillar Electronic Unit Injector (EUI), and a prototype "Next Generation Injector" (NGEUI) capable of ultra-high pressure split injections.

A mathematical declaration of the optimization goal is stated using an objective function similar to that used by Senecal et al. [1, 2], and the optimization process is reduced to a problem of searching for a minimum or maximum on a response surface. The variables included in the optimization process included injection pressure, boost pressure, EGR rate, injection timing, and split injection parameters. Using the response surface optimization scheme, the engine could be optimized rapidly, yielding both reductions in emissions consistent with future heavy-duty standards, and also a substantial reduction in fuel consumption compared to the same engine using the electronic unit injector (EUI) which was calibrated for 1998 emissions levels, as shown in Fig. 2.

Through use of an optimized double injection with optimized levels of boost and EGR an emissions level of 2.31 g/kW-h $\text{NO}_x + \text{HC}$ with 0.045 g/kW-h particulate was achieved with a brake specific fuel consumption of 239 g/kW-h. These emissions values are consistent with 2004 US EPA emissions levels and the optimized configuration's BSFC is a 7% improvement over the baseline EUI's BSFC. Further, the present work demonstrates that RSM optimization is an effective method for optimizing engine operating parameters.

Multi-dimensional Simulation of Diesel Engine Cold-Start

The complex physical processes occurring during cold starting of diesel engines mandate the use of advanced physical submodels in computations. The present study utilized a continuous probability density function to more fully represent the range of compositions of commercial fuels [5]. The model was applied to single droplet calculations to validate the predictions against experimental results. Analysis of a high-pressure diesel spray showed axial composition gradients within the spray. Previous wall-film modeling was extended to include the continuous multi-component fuel representation. Using these models, the cold-start behaviour of a heavy-duty diesel engine was analyzed. The predictions show that multi-component fuel modeling is critical to capturing realistic vaporization trends. In addition, the

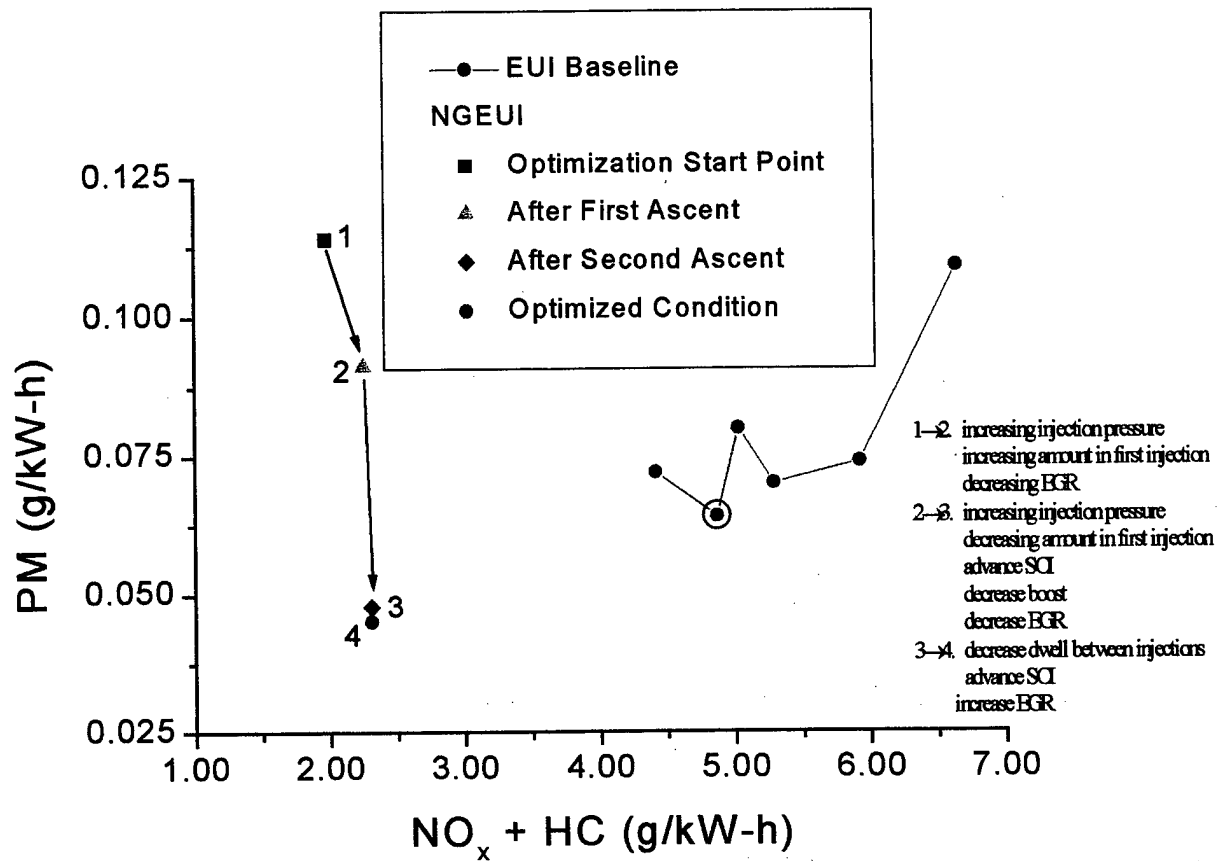


Figure 2 Measured Particulate and NO_x for a heavy-duty diesel engine operating at 57% load, 1757 rev/min using the Response Surface optimization technique. Point 4 shows the optimum point.

spray-film interaction modeling is crucial to capturing the spray impingement and subsequent secondary atomization. Heating the intake air temperature was shown to result in reduced ignition delay and accelerated vaporization. Increasing the fuel temperature increases vaporization prior to and away from the initial heat release. Increasing the injection pressure increased vaporization without much change in the ignition delay. Split injections, with 75% of the fuel contained in the second pulse, displayed a substantial reduction in ignition delay due to the ignition of the first pulse. The timing of the first injection was found to be an important parameter due to differences in the spray impingement behavior with different timings [6].

Comparisons of Predicted Diesel Spray Liquid Penetration with Optical Measurements

The performance of two spray models for predicting liquid and vapor fuel distribution, combustion and emissions was investigated. The model predictions were compared with extensive data from in-cylinder

laser diagnostics carried out in an optically accessible heavy-duty, D. I. diesel engine over a wide range of operating conditions [7]. Top-dead-center temperature and density were varied between 800 K and 1100 K and 11.1 and 33.2 kg/m³, respectively. Two spray breakup mechanisms were considered: due to Kelvin-Helmholtz (KH) instabilities and to Rayleigh-Taylor (RT) instabilities. Comparisons of a wide range of parameters, which include in-cylinder pressure, apparent heat release rate, liquid fuel penetration, vapor distribution and soot distribution, have shown that a combination of the KH and the RT mechanisms gives realistic predictions. In particular, the limited liquid fuel penetration observed experimentally was captured by including these two competing mechanisms in the spray model, as shown in Fig. 3. Furthermore, the penetration of the vapor fuel ahead of the liquid spray was also captured. A region of high soot concentration at the spray tip was observed experimentally and also predicted by the KH-RT spray breakup model.

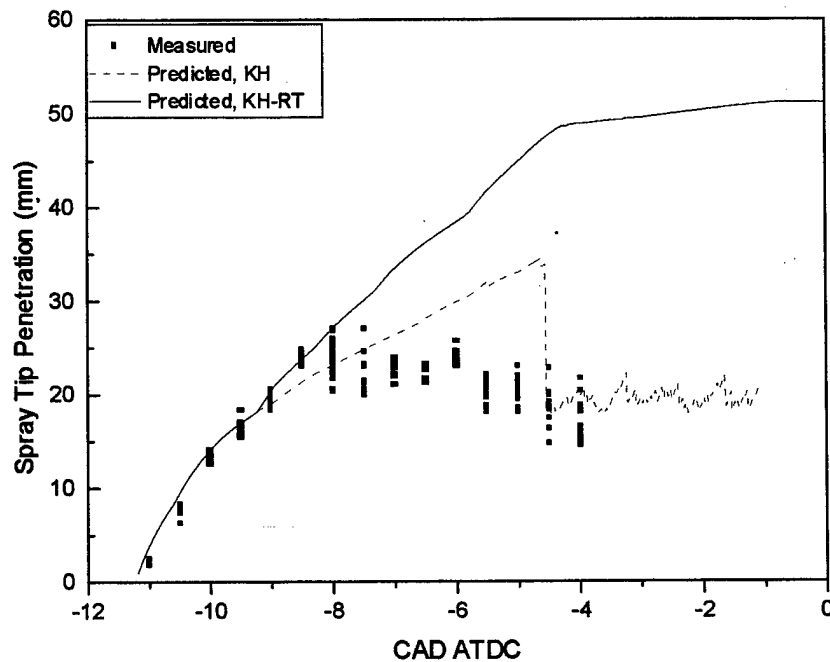


Figure 3 Liquid fuel penetration as predicted by KH and KH-RT model and measured in the Sandia optical engine for the baseline operating condition.

Modeling the Effect of Premixed Combustion on Diesel Engine NOx

The effect of the premixed burn on NOx production in heavy-duty diesel engines was investigated computationally. Previously it was thought that the premixed burn controlled the NOx production. However, recent experiments have suggested that NOx production in modern diesel engines originates in the diffusion burn period. A modified version of the ERC KIVA-3 code was used, and techniques were developed to track the NOx produced during the different phases of combustion. The study was conducted for a Cummins N-14 engine and for a Caterpillar 3406 engine, with and without swirl. The results show that in engines without significant swirl, the NOx is formed from the diffusion burn, and also from the air entrainment process that occurs at the tail of the spray at the end of injection. Most of the NOx is formed at the periphery of the spray, and very little new NOx is formed after the end of combustion. However, with swirl, the NOx forming regions are swept downstream, and significant NOx is formed from the premixed burn. In addition, the upstream portion of the diffusion flame produces very little NOx. These processes are depicted in the model shown in Fig. 4.

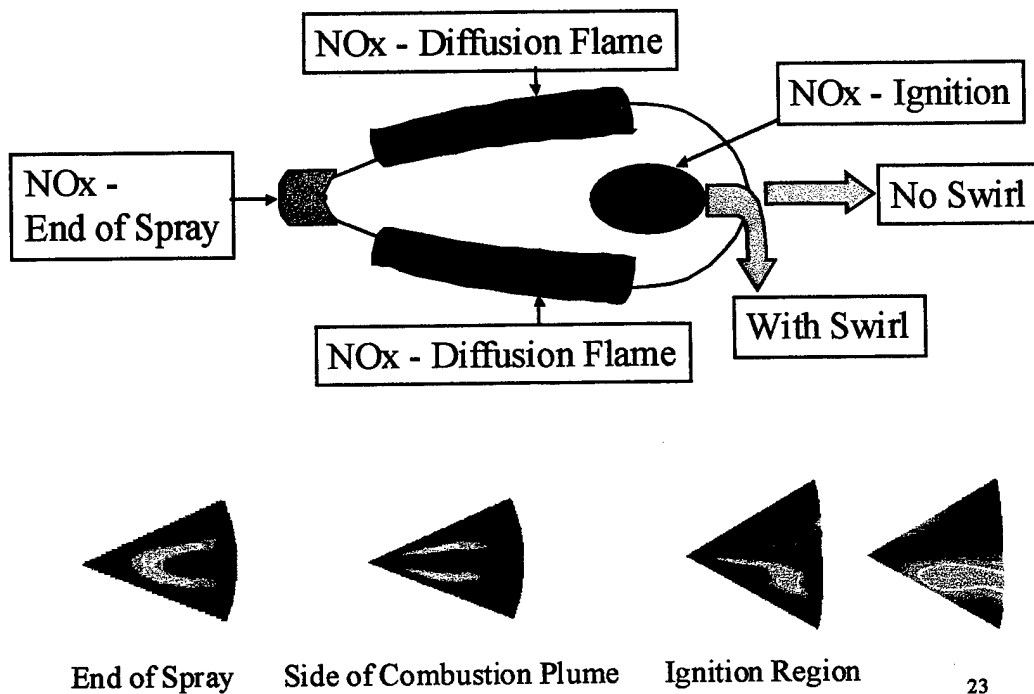


Figure 4 Conceptual picture of NOx formation mechanisms in a heavy-duty diesel engine

References

1. Senecal, P.K., and Reitz, R.D., "Simultaneous Reduction of Emissions and Fuel Consumption using Genetic Algorithms and Multi-dimensional Spray and Combustion Modeling," Submitted SAE Spring Fuels and Lubricants Meeting, Paris, June 19-22, 2000.
2. Senecal, P.K., Montgomery, D.T., and Reitz, R.D., "A Methodology for Engine design using Multi-dimensional Modeling and Genetic Algorithms with Validation through Experiments," Submitted for Publication, Int. Journal of Engine Research, 2000.
3. Reitz, R.D., "Controlling D.I. Diesel Emissions Using Multiple Injections and EGR," Combust. Sci. and Tech. V. 138, 1-6, p. 257, 1998.
4. Montgomery, D.T. and Reitz, R.D., "Optimization of Heavy-Duty Diesel Engine Operating Parameters Using A Response Surface Method," Submitted SAE Spring Fuels and Lubricants Meeting, Paris, June 19-22, 2000.
5. Lippert, A.M., Stanton, D.W., Rutland, C.J., Hallett, W.L.H., and Reitz, R.D., "Multi-dimensional Simulation of Diesel Engine Cold-Start with Advanced Physical Submodels," Accepted for Publication, Int. Journal of Engine Research, 2000.
6. Lippert, A.M., Stanton, D.W., Rutland, C.J., and Reitz, R.D., Hallett, W.H.L., "Investigating the Effect of Spray Targeting and Impingement on Diesel Engine Cold Start," SAE Paper 2000-01-0269, 2000.
7. Ricart, L.M., Reitz, R.D., and Dec, J.E., "Comparisons of Predicted Diesel Spray Liquid Penetration and Vapor Fuel Distributions with In-Cylinder Optical Measurements," Accepted for ASME Transactions, 1999.

Planar Reacting Shear Layer

Students: Darius Mehri, Steve Boucher, Marcus O'Brien, Lyle Pickett

A planar reacting shear layer apparatus has been designed, constructed and used to investigate mixing-controlled combustion of hydrocarbon fuels over a range of chemical and mixing rate conditions. The flow conditioning elements and the test section are enclosed in a pressure vessel which is capable of operation up to 6 atm. Control of the inlet stream mass flow rates determines the strength of the shear between the two streams, which in turn governs the mixing rate of the two streams. In addition, the composition and temperature of the two streams can be adjusted to vary the global reaction rate. Typical operation has one stream as the oxidizer (air) which is preheated, and the other stream is fuel diluted in argon and is unheated.

A considerable effort was undertaken to benchmark the facility against previous results in the literature for non-reacting conditions since it is known that the initial conditions are important in the development of the shear layer. Hot wire anemometry measurements of the mean velocity showed a self-similar profile for distance of 250θ , where θ is the momentum thickness of the boundary layer at the tip of the splitter plate.

In addition, high speed shadowgraph movies verified the existence of large-scale structures in the mixing layer and their dynamics.

In order to investigate the mixing characteristics of the shear layer, passive scalar measurements were made under non-reacting conditions. Acetone was seeded into the high speed free stream, and planar laser-induced fluorescence measurements were performed. Large data sets were acquired and statistical quantities were derived from the measured results. Figure 1 a) shows an instantaneous image of the passive scalar field. The large scale Kelvin-Helmholtz structures are clearly evident, and the layer is seen to be at the turbulent transition point, which for this facility occurs near a local Reynolds number of approximately 5000. Figure 1 b) and c) show probability density functions for two conditions with a local Re of 5000, where the high speed boundary layer in 1 c) was tripped to produce turbulent inlet flow conditions. In Figure 1 b) the pdf shows a preferred mixture composition within the layer which is consistent with the high speed entrainment bias of shear layer flows. However, the turbulent inlet conditions produce a significantly different mixing behavior. The pdf displays a marching shape where no preferred mixture composition is obtained. A similar result was obtained when the high speed boundary layer was naturally turbulent. It is believed that turbulence in the inlet streams inhibits the growth of the initial Kelvin-Helmholtz instability, thus modifying the mixing characteristics in the layer.

Combustion was initiated by using a swirl burner at the splitter plate tip. Once combustion was engaged, the burner was turned off, and self-sustaining combustion was achieved. The mixing and combustion processes were investigated using planar imaging diagnostics. Laser-induced fluorescence of OH was used as a marker of the combustion zone. An interference signal, which was determined to be the laser-induced incandescence of soot, was found to be an excellent marker of the parent fuel (as confirmed by acetone fluorescence experiments). Several interesting results have been obtained with this system. Figure 2 shows the resulting flame morphology and fuel mixing for a case where the free stream velocities were held constant, but the fuel was switched from the high speed stream (a) to the low speed stream (b). Also shown are the results obtained from the nonreacting case. In the case where the fuel is in the high speed stream the flame remains relatively unaffected by the fluid flow, and the rollup frequency of the structures occurs at a higher frequency than the non-reacting case. However, for the case where fuel is in the low speed stream, the flame sheet is convected by the flow, and the rollup frequency is decreased from the non-reacting case. In the former case it is observed that an internal mixing layer is formed between the reaction surface at low density, and the fuel stream at high density. This observed result agrees with theoretical predictions of the most amplified instability wavelength for shear layers with density variations. It is important to note that the observed flame shape differences is not related to a 'laminarization' due to the increase in temperature as both cases have the same stoichiometry, and hence flame temperature.

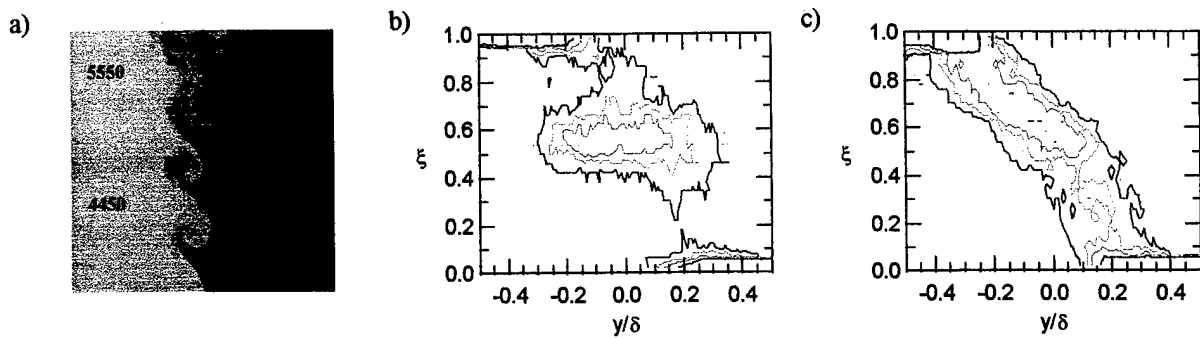


Figure 1 Passive scalar results for a case with $U_1=3$ m/s, $r=0.4$, (a) instantaneous mixture fraction where the numbers shown are the local Reynolds number, (b) mixture fraction pdf, (c) mixture fraction pdf with a tripped boundary layer.

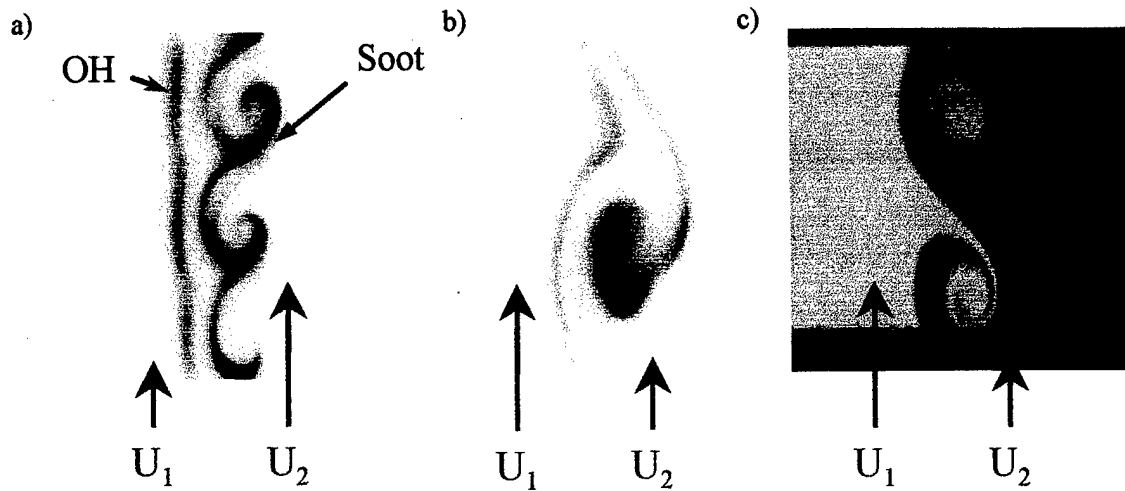


Figure 2 Laser-induced fluorescence images of OH, which distinguishes the reaction zone, and laser-induced incandescence of soot, which distinguishes the parent fuel boundary, for a case with $U_1=2$ m/s, $r=0.4$ and propane as the fuel, (a) fuel on the high speed side, (b) fuel on the low speed side, and (c) non-reacting result at the same condition.

Calibration of the Laser-Induced Fluorescence Technique for Measuring Oil Film Thickness at the Ring Reversal Region of a SI Engine by Using Capacitance Gauges

A direct calibration of the laser-induced fluorescence technique for measuring oil film thickness was achieved by performing simultaneous capacitance measurements of the minimum oil film thickness of the top piston ring. The minimum film thickness determined from the capacitance technique has a high level of confidence due to the minimal curvature of the top ring, and the fully flooded conditions which can be expected at the minimum film location. The distance derived from the capacitance measurement was used as a direct calibration of the voltage signal of the photomultiplier tube used for the fluorescence detection. A rigorous error analysis was performed, and the results from this technique were also compared to the subjective technique of ring profile matching.

The simultaneous measurement of film thickness by two methods provided further insight into the nature of the ring-oil interaction. In particular, the conditions at the trailing edge of the ring were elucidated. The oil film appears to separate from the ring face, rather than cavitate as has been suggested in the literature. At the point of separation, the fluorescence signal is seen to decrease, while the predicted distance from the capacitance data increases significantly. The increase in the capacitance-derived distance is due to the sudden decrease in the dielectric constant due to the absence of oil. The fluorescence signal was found to increase again after the ring passed due to the presence of oil adhere to the piston. The direct calibration method has proven to be the most reliable method available, and has been adopted in all subsequent work.

Demonstration of a Diagonal Excitation/Observation Technique for Laser Induced Fluorescence of the CH Radical in Atmospheric Pressure Flames

Background

Planar laser-induced fluorescence (PLIF) of the CH radical is an optical technique which can be used to determine the location of the reaction zone in combustions flows.¹ CH is typically found in a relatively thin region near the leading edge of reaction zones, making it an excellent marker for determination of flame structure.² Two-dimensional spatial distributions of CH fluorescence can be used to measure scales of combustion structures, flame thickness, and evidence of interaction with turbulence. However, application of PLIF of CH is challenging because of the unique character of the quantum transitions of the CH molecule.

The CH PLIF technique presented here is intended for the high pressure combustion environment in Diesel engines. In the regime of high-pressure combustion, saturation of the CH transition is usually not possible due to line broadening and extreme collisional quenching. In the absence of saturation, the excitation efficiency and resulting fluorescence signal are proportional to the oscillator strength of the transition.

The $A^2\Delta \leftrightarrow X^2\Pi$ electronic transition of the CH molecule is extremely diagonal. The oscillator strengths of transitions for which the vibrational quantum state does not change ($v'=v''$) are at least 2 orders of magnitude stronger than the off-diagonal transitions for which the vibrational state changes during an electronic transition ($v' \neq v''$).³ In high quenching environments like Diesel combustion for which PLIF of CH is limited by the transition strength, excitation/observation in diagonal bands is therefore preferable. The rotational branches of the diagonal (0,0), (1,1) and (2,2) vibrational bands, however, are spectrally overlapped within the wavelength interval of 415 nm to 445 nm.⁴ Application of a filtering scheme which rejects elastic scatter while efficiently collecting fluorescence emission in the same diagonal band can therefore be difficult, due to the necessarily small spectral separation between excitation and observation. Although the transition strengths of off-diagonal bands are weaker, excitation or observation in off-diagonal bands is more attractive for spectral filtering, due to the greater spectral separation of excitation and emission wavelengths. Given the diagonal nature of the CH transition, three different classes of PLIF of CH have been demonstrated, as reviewed by Paul and Dec².

- **Diagonal eXcitation with Off-diagonal Collection (DX/OC):** Namazian performed PLIF of CH with excitation in the Q-branch of the (0,0) diagonal vibrational band near 431 nm using a flashlamp-pumped dye laser.^{5,6} The 1.8 ms pulse was formed into a sheet using a multipass cell, providing a sheet intensity 30 times that of lens-formed sheets. The resulting fluorescence emission was collected in the off-diagonal (0,1) vibrational band near 489 nm. Since the excitation and collection wavelengths were separated by over 50 nm, a conventional 10 nm wide dielectric bandpass filter centered at 490 nm transmitted the fluorescence emission while rejecting the elastic scatter. The diagonal excitation strategy of this technique provides relatively high excitation efficiency, but the because of the weak oscillator strength of the (0,1) off-diagonal vibration band, the resulting fluorescence emission is two orders of magnitude weaker than that of a diagonal band. In experiments that are limited by signal strength, this off-diagonal strategy is at a disadvantage to techniques which employ a diagonal band for observation.
- **Off-Diagonal eXcitation with Diagonal Collection (OX/DC):** Paul and Dec mixed the fundamental output of a YAG-pumped dye laser operating with Rhodamine 640 with the leftover YAG fundamental, exciting the CH molecules in the off-diagonal (1,0) vibrational band near 387 nm². A long pass filter was employed to reject elastic scatter while allowing observation of the resulting fluorescence emission in the (0,0) and (1,1) diagonal bands near 431 nm. The authors believed that emission from the (0,0) band was possible because of vibrational energy transfer from the $v'=1$ state to the $v'=0$ state. Since this technique collects radiation from diagonal bands, the potential signal collected per excited molecule is the highest possible. In saturating conditions, the excitation efficiency of this off-diagonal technique is nearly as high as that of techniques which use diagonal excitation, and the spectral filtering is straightforward. In non-saturating conditions with high

quenching however, the excitation efficiency of the off-diagonal excitation can be two orders of magnitude less than techniques which employ diagonal excitation.

- **Diagonal eXcitation with Diagonal Collection (DX/DC):** Allen et al. performed PLIF of CH with both excitation and observation in the same vibrational band.⁷ Excitation was performed in the R-branch of the (0,0) band near 428 using a YAG-pumped dye laser operating with Stilbene 420. The resulting fluorescence signal was observed in the Q-branch of the (0,0) band near 431 nm. Because of the narrow spectral separation of the excitation and emission wavelengths, a custom 3-cavity interference filter was constructed to pass the fluorescence emission while rejecting elastic scatter. The interference filter was constructed with a center wavelength of 431.5 nm, having a bandwidth of 1 nm. While this technique utilized diagonal bands for both excitation and emission and therefore had the greatest potential for high signal strengths, the filtering scheme accepted only a small portion of the available fluorescence emission, limiting the sensitivity of the technique.

The DX/DC-HNF Technique:

Here we demonstrate a DX/DC technique with a new, more efficient filtering scheme. A Kaiser Optical Holographic Notch Plus Filter (HNF) was employed to reject elastic scatter of laser radiation while allowing efficient collection of fluorescence emission as near as 5 nm away. The HNF has a transmission of 10^{-6} at the central wavelength, while having a transmission of up to 50% outside the ~8 nm FWHM bandwidth of the notch. Thermal emission, fluorescence, and chemiluminescence of other species may be present and may obscure the CH fluorescence signal. An additional conventional dielectric bandpass filter (BPF) may be employed to spectrally isolate the CH fluorescence emission from these other sources. Using the HNF in combination with a dielectric 10 nm wide bandpass filter, elastically scattered laser light may be sufficiently rejected while fluorescence within the CH diagonal emission band is collected.

A computer simulation of the excitation/emission process which accounted for saturation effects, Doppler and pressure broadening of absorption lines, relative oscillator strengths of rotational branches and diagonal bands, and population distributions of the ground and excited states was created. The simulation was used as a design tool to determine the best combination of HNF and BPF center wavelengths under a wide spectrum of pressure, temperature, and quenching environments.⁸ Under conditions typical of Diesel engine combustion, it was found that excitation in the R-branch of the (0,0) vibrational band near 424.4 nm with observation centered at 431 nm provided the highest possible fluorescence signal strength. With laser excitation at 424.4 nm, about 8% of the available fluorescence emission from the diagonal bands between 428 nm and 438 nm is transmitted through the HNF/BPF filter set. In the experiments presented here, it was not necessary to include the BPF, since significant spectral interference was not present. Some chemiluminescence emission from C_2 radicals, however, was present from 465 nm to 565 nm, so a short-wave pass filter (SPF) with a cutoff wavelength of ~500 nm was employed to remove some of this emission while transmitting ~80 % of the CH fluorescence. With the substitution of the SPF for the BPF, the total

transmission of emission in the Q- and P- branches increased to 20 %. This represents an increase in signal strength by at least a factor of 25 over off-diagonal excitation experiments in non-saturating conditions typical of Diesel combustion, due to the higher strength of the diagonal transitions.⁸

Experimental:

A Continuum Powerlite 8010 Nd:YAG laser tuned to deliver 200 mJ at 355 nm in a 6 ns pulse was used to pump a Lambda Physik Scanmate 2E dye laser operating with Stilbene 3 laser dye. Although the computer simulation indicated optimum excitation for Diesel engine conditions at 424.4 nm in the (0,0) band, comparable signal strength could be obtained for nearby lines, such as those near 425 nm. Significantly higher dye laser efficiency could be obtained operating near 425 nm, so excitation was performed in the R-branch at the $R_{1f}(10.5)$ line. Over 30 mJ per pulse at 425.015 nm was attainable using the fundamental output of the dye laser.

PLIF of CH was performed in two different flames produced by two different burners for a variety of flow velocities and mixture strengths. A Victor 4-UM-1 oxyacetylene torch with a 860 μm exit diameter (No. 0 tip) produced a premixed oxyacetylene flame with a ~ 7 mm high inner cone. The torch was operated in a room temperature environment at atmospheric pressure and was oriented so that the premixed oxygen and acetylene exited vertically upward. The vertical laser sheet passed through the central axis of the flame, and the resulting fluorescence emission was collected at a right angle to the sheet, as shown in Fig 1. The sheet forming optics for this flame, shown in Fig 2, produced a vertical laser sheet approximately 10 mm high and 250 μm wide.

The technique was also applied to a premixed propane-air flame produced by an 11 mm diameter Bunsen burner. The burner used a 4-hole collar for flame stabilization. This burner was also operated in laboratory air at room temperature and atmospheric pressure, with the gases exiting vertically upward. The Bunsen burner produced a much taller flame (20 - 200 mm) than the oxyacetylene torch, and a different set of sheet forming optics were used, as shown in Fig 2. These optics produced a laser sheet ~ 20 mm high and about 250 μm wide.

Since the HNF is angle tunable, it should receive parallel rays for best rejection of elastic scatter. An $f/2$ lens systems operating at an infinite conjugate ratio consisting of a 150 mm F.L. object lens and a 300 mm F.L. image lens, having a magnification of 2, was constructed for the oxyacetylene torch images. The HNF and SPF were placed between the two achromatic lenses. For the propane-air flame, a 150 mm F.L. lens was substituted for the image lens, which yielded an $f/1.5$ system with a unity magnification. The SPF was unnecessary for the propane-air flame, since significant C_2 emission was not present. Both lens systems allowed partial collimation of the ~ 13 mm wide field, providing a maximum half angle divergence of 2.5° to the HNF, minimizing the angle tuning effects.

The images were acquired with an EOSI 9437/25 gated, intensified CID camera system. The fluorescence emission in the laser sheet was imaged onto the face of a DEP PP 0340 image intensifier. The intensifier was coupled to a CidTech 3710-D CID camera via a fiber optic taper. The intensifier was operated at full gain, with a gate width of approximately 50 ns. The intensifier was equipped with a S-20 photocathode and a P-43 phosphor screen. The quantum efficiencies at 430 nm of the photocathode and the phosphor were ~20 % and ~30 % respectively. The electronic gain of the intensifier was 30,000 yielding a total photon gain of about 1500. The digital camera image was transferred via analog video to a Data Translation 2862-SQ-60Hz frame grabber with a 8 bit pixel depth in a 512x480 field format. Using a Newport RES-1 backlit resolution target, the 4% transfer function resolution of the entire system, including intensifier operating at maximum gain, camera, and frame grabber was determined to be 6 lp/mm on the input face of the intensifier. The system could therefore resolve features in the plane of the laser sheet as small as ~40 μm for the oxyacetylene images and ~80 μm for the propane-air images.

The YAG laser was necessarily operated at a 10 Hz pulse rate to maintain the stability and quality of the output beam for proper operation of the dye laser. Since the 30 Hz frame rate of the synchronized camera-frame grabber was fixed and unchangeable, the camera acted as the master timing source for the system. Using a IBM compatible PC equipped with a CIO-CTR-10 1 MHz counter card, the camera frame rate divided by 3 to generate 10 Hz flashlamp and Q-switch trigger pulses for the YAG laser. The ~50 ns wide intensifier gate was timed to encompass the 6 ns dye laser pulse using a one-shot delayed pulse generator circuit. The laser was timed to fire between image frames, allowing the camera to operate normally at 30 Hz, while every third frame contained a fluorescence image. The fluorescence digital images from the frame grabber were saved to the hard disk of the PC, which reduced the overall acquisition rate to approximately 1 frame per second, due to the write time to the hard disk.

Results and Discussion:

Images were acquired at a variety of cold flow Re_D -equivalence ratio combinations. By adjusting the equivalence ratio, the degree of lifting for the oxyacetylene flame could be varied from completely attached to partially lifting to completely lifted. Even with the high collection efficiency of this filtering scheme, the images were quite dark, registering about 20 out of 255 counts per pixel at maximum gain. There is a good deal of noise ($S/N \approx 10$) in the raw images when the intensifier is at maximum gain, as well as a significant black level offset (~12 counts).

A post-processing scheme was implemented to improve contrast, remove the background offset, and remove some of the random intensifier noise. The contrast was improved through a simple linear scaling of all pixels. A least squared fit to a linear intensity variation across the entire image provided an estimate of the background offset. This function was subtracted from the image to remove the background offset. Finally, the image was fit to a second order polynomial of the form:

$$I_{i,j} = Ai^2 + Bj^2 + Cij + Di + Ej + F \quad (1)$$

where $I_{i,j}$ is the intensity of the pixel at coordinates i,j and $A, B, C, D, E,$ and F are the fit constants. This function was chosen because it provides for 2-D intensity variations such as parabolic troughs, inclined planes, saddles, and paraboloids of revolution. A least squares fit to Eq (1) at each pixel was performed, including pixels within a circular region about as wide as the observed flame fronts. This allowed the maximum smoothing of the noise, without smearing any of the observed structures. This is the first step of a post-processing scheme, which will be extended in the future to identify and quantify flame structures.

Post-processed images for the oxyacetylene flame at $Re_D=8000$ and $\Phi=0.46$ are shown in Fig 3. The four images on the left were acquired with the laser tuned onto the $R_{11}(10.5)$ CH absorption line at 425.015 nm. The four images on the right were acquired with the laser tuned to 425.300 nm, which is between the CH absorption lines, and should produce no CH fluorescence. The distance above the tip of the torch (in mm) is given in the scale to the left of each group of images.

This flame was characterized as a partially lifting flame. The flame was attached for about $\frac{3}{4}$ of the circumference of the nozzle exit on the right side of the image, while it was beginning to lift along about $\frac{1}{4}$ of the circumference on the left side of the images. The degree of lifting was most dramatically affected by the equivalence ratio. The flame could be made to change from completely attached to partial lifting to severe lifting to blow-off with only slight variations of the equivalence ratio from $\Phi=0.5$ to $\Phi=0.4$.

There was significant emission in the off-line images on the right side of Fig. 3. Ideally, there should be no signal gathered when the laser is tuned off the CH line. There was no signal present in the absence of a laser pulse, indicating that the signal is laser generated, and is not merely natural flame emission. The spatial location of the offline emission seems to be the same as that of the online emission. This was very evident in laminar flames, which are steady and provide repeatable images from frame to frame. Therefore, it appears that the source of the offline emission was in the same spatial location as the CH molecules. An emission spectrum, collected using a spectrometer focussed on a single point within the laser sheet, indicated that the signal is not due to elastic scatter of the laser line passing through the filters, but rather to broadband red shifted emission. The broadband emission was observed regardless of the tuning of the laser within the output spectrum of the Stilbene 3 laser dye, and hence was due to some laser-induced interaction other than single-line pumped CH fluorescence. Such broadband emission has been observed in other PLIF studies, and has been attributed to fluorescence of PAH's in the flame.^{7,9,10}

CH fluorescence images for the propane-air flame at $Re_D=2000$ and $\Phi=1.4$ are shown in Fig 4. Again, the online images are on the left, and the offline images are on the right. The images were acquired at three different heights for this flame, since the field of view was not large enough to image the entire flame.

Since the images were acquired at a rate of only 1 Hz and at completely different times, there is no continuity between images at different heights for the propane-air flame. The distance above the burner tip (in mm) is again given on the left of each set of images.

In the propane-air images, there was emission present in the off-line images, but it was not as strong as in the oxyacetylene images. This behavior was observed for all flow conditions studied. This seems to indicate that the strength of the off-line signal is a function of the composition of the fuel. The spatial distribution of the off-line emission again appears to be very similar to that of the online CH images.

This technique as applied here was nearly signal limited. The intensifier was operated at its maximum gain for all images. Even at maximum gain, the fluorescence signals utilized only 10% of the full range of the CID camera, and post-processing was necessary to enhance the images.

These results fulfill the objective of determining the instantaneous spatial distribution of the CH radical within a reacting flow. In future work, these images will be used to generate flame "skeletons," which represent the spatial location of the center of the flame fronts. The flame skeletons will be interrogated to determine such quantities as flame curvature, flame thickness, and scales of turbulent structures.

Conclusions:

A diagonal excitation/observation strategy for planar laser-induced fluorescence of the CH radical was demonstrated in atmospheric pressure premixed oxy-acetylene and propane-air flames. Excitation was performed in the R-branch of the (0,0) band at 425.015 nm and a holographic notch filter was utilized to reject elastic scatter at this wavelength. Fluorescence emission was collected in the Q- and P- branches from 428 nm to 440 nm in the same (0,0) band. A short-wave pass filter was employed to remove C₂ emission when probing the oxyacetylene flame.

This configuration provides a fluorescence signal strength that is 25 times larger than previous off-diagonal techniques. Satisfactory images of the spatial distributions of the CH radical were obtained in both flames. Even at maximum intensifier gain, the signals were weak, registering only 20 counts out of the available 256 count range of the camera. Significant broadband, red-shifted laser-induced interference was present even when the laser was tuned off the CH absorption line, and is probably due to PAH fluorescence.

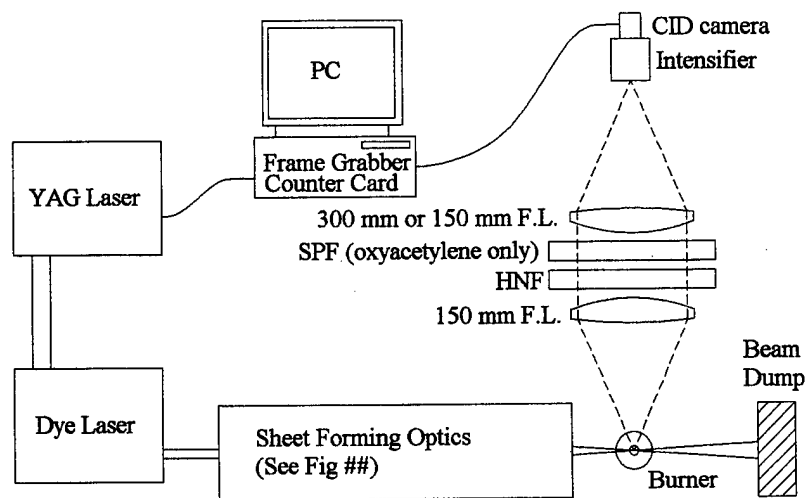


Figure 1: Experimental layout for PLIF of CH

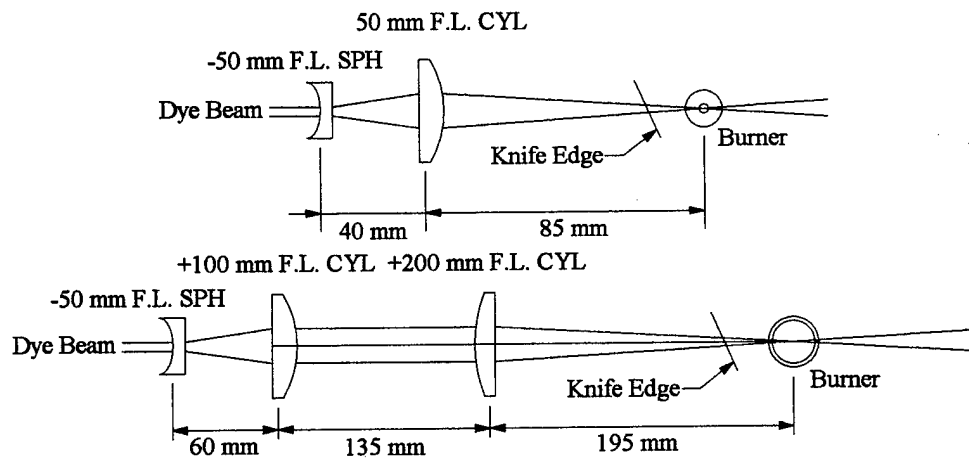
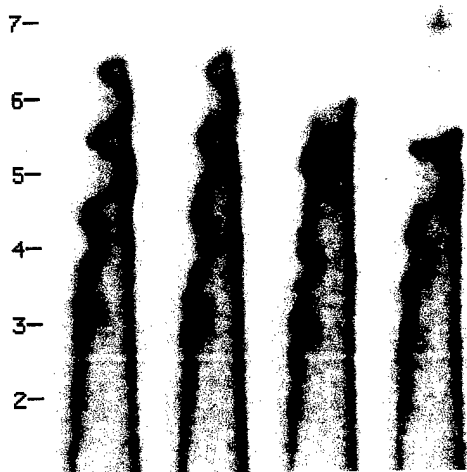


Figure 2: Sheet forming optics for oxyacetylene flame (top) and propane-air flame (bottom).

Laser tuned on CH line (425.015 nm)



Laser tuned off CH line (425.3 nm)

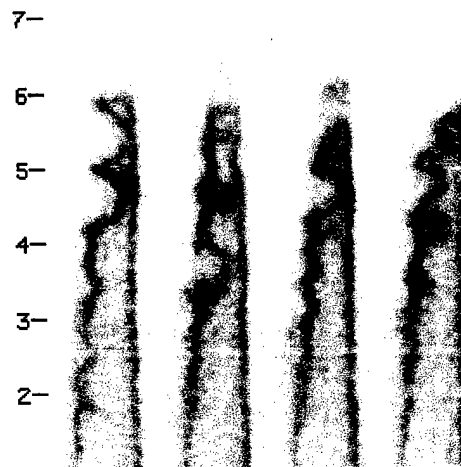
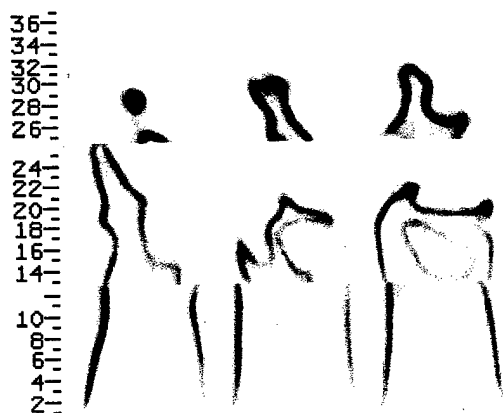


Figure 3: CH PLIF images for premixed oxy-acetylene torch at $Re_D=8000$ and $\Phi=0.46$. The scale to the left is the distance above the torch tip, in mm.

Laser tuned on CH line (425.015 nm)



Laser tuned off CH line (425.3 nm)

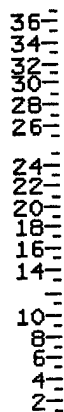


Figure 4: CH PLIF images for premixed propane-air Bunsen Burner at $Re_D=2000$ and $\Phi=1.4$. The scale to the left is the distance above the burner tip, in mm.

References:

1. R. W. Schefer, M. Namazian and J. Kelly, "CH, OH and CH₄ Concentration Measurements in a Lifted Turbulent-Jet Flame," Twenty-Third Symposium (International) on Combustion/The Combustion Institute, 669-676 (1990).
2. P. H. Paul and J. E. Dec, "Imaging of Reaction Zones in Hydrocarbon-Air Flames by use of Planar Laser-Induced Fluorescence of CH," *Opt. Lett.* **19**, 998-1000 (1994).
3. A. Bembenek, R. Kepa, A. Para, M. Rytel, M. Zachwieja, J. D. Janjic and E. Marx, "Reinvestigations of the A²Δ-X²Π Band System in the CH Radical," *J. Mol. Spect.* **139**, 1-10 (1990).
4. P. F. Bernath, C. R. Brazier, T. Olsen, R. Hailey, W. T. M. L. Fernando, C. Woods and J. L. Hardwick, "Spectroscopy of the CH Free Radical," *J. Mol. Spect.* **147**, 16-26 (1991).
5. M. Namazian, R. L. Schmitt and M. B. Long, "Two-Wavelength Single Laser CH and CH₄ Imaging in a Lifted Turbulent Diffusion Flame," *App. Op.* **27**, 3597-3600 (1988).
6. M. Namazian, J. T. Kelly and R. W. Schefer "Near Field Instantaneous Flame and Fuel Concentration Structures," Twenty-Second Symposium (International) on Combustion/The Combustion Institute, 627-634 (1988).
7. M. G. Allen, R. D. Howe and R. K. Hanson, "Digital Imaging of Reaction Zones in Hydrocarbon-Air Flames using Planar Laser-Induced Fluorescence of CH and C₂," *Op. Lett.* **11**, 126-128 (1986).
8. M. P. Musculus and D. E. Foster, "Development of a Filtering Technique for Planar Laser-Induced Fluorescence of the CH Radical with Diagonal Excitation/Observation," Submitted to *Applied Spectroscopy*.
9. J. E. Dec and E. B. Coy, "OH Radical Imaging in a DI Diesel Engine and the Structure of the Early Diffusion Flame," SAE Paper 960831, International Congress and Exposition (1996).
10. F. E. Tichy, T. Bjorge, B. F. Magnussen, P. E. Bengtsson and F. Mauss, "Two-Dimensional Imaging of Glyoxal (C₂H₂O₂) in Acetylene Flames using Laser-Induced Fluorescence," *Appl. Phys. B.* **66**, 115-119 (1998).

Parameters That Affect the Impact of Auxiliary Gas Injection in a DI Diesel Engine

Brief Summary

The maximum power density that can be obtained from current diesel engines is typically limited by the constraint on smoke emissions, i.e. smoke limited. In this research effort we investigated the potential to increase the maximum power out of the engine by inducing additional air fuel mixing during expansion stroke of the engine. This portion of the burning is usually referred to as mixing controlled. We did this by invoking an auxiliary gas injection (AGI) system. Experiments were conducted using various gas injection directions and compositions to explore the effect of these parameters. Numerical simulations were employed to provide additional insight. The potential of auxiliary gas injection to facilitate an increased power density was assessed by its ability to decrease soot emissions. Nitrogen oxide emissions were also monitored during the experiments. AGI direction was found to have a profound impact on soot emissions. It is our hypothesis that this was due to changes in the fuel spray-gas jet interaction with injection direction. Simulations supported this theory and suggested that the number of soot clouds affected by the gas jet may also be a factor. The oxygen content of the gas jet was also found to have an influence on emissions. Researchers found that, when the oxygen content of the gas jet was increased, soot emissions decreased. However, this was found to have a detrimental affect on NO. This was believed to stem from the fact that a portion of the injected gas was entrained causing it to have a direct impact on the composition inside the fuel spray where most of the soot chemistry takes place.

BACKGROUND

Since nitrogen oxides (NO_x) and particulates (soot) are considered hazardous, both to the environment and to human health, legislation exists in most developed industrial nations regulating their output. Current commercial engines are limited in their operating range by constraints of meeting soot and NO_x emission levels. Usually strategies used to affect a decrease in one of these emissions causes an increase in the other. As these standards become more stringent the limits on peak power density become more severe. It is becoming increasingly important to find methods to overcome this soot- NO_x tradeoff.

It has been demonstrated that one way to realize this objective is to increase in-cylinder turbulence during the latter portion of combustion [1-8]. In six separate studies, researchers using various forms of gas jet intrusion to enhance mixing (e.g. air cells, gas injection) reported significant reductions in soot emissions, typically accompanied by no change or a slight drop in NO_x . Evidence from these studies indicates that the drop in soot is a result of an increase in soot oxidation brought about by the increased turbulent mixing. It has been suggested that NO_x is not adversely affected because the mixing occurs at a time when NO_x chemistry is already frozen. [1-8]

Although the benefits of increasing in-cylinder turbulence have been well demonstrated, the factors that dictate its impact are still not well understood. In a previous publication [1], the authors established that increasing mixing is only effective in operating regimes in which the in-cylinder turbulence is insufficient to enable adequate fuel-air mixing. It was also shown that even when operating in this regime, dubbed "under-mixed", the increase in mixing is not always beneficial.

The purpose of this paper is to explore some of the parameters that may be important in determining whether increasing the mixing is beneficial or detrimental in this "under-mixed" regime. Two parameters will be discussed: the direction and the oxygen content of the gas jet used to generate turbulent mixing. It has been suggested that the direction of the gas jet is particularly important in this system because it dictates the nature of the interaction between the gas jet and the fuel spray. The authors contended that it was this interaction that determines the impact of enhancing the mixing [1].

Evidence supporting this theory was generated by Kamimoto *et al.* [2,3] who installed an air cell on a naturally aspirated, direction injection diesel engine. An air cell is a small chamber connected to the combustion chamber via a small passage. Air flows into the air cell while the combustion chamber pressure rises; however, once peak pressure is attained a gas jet emerges from the air cell, thus stirring the cylinder contents. Kamimoto *et al.* found that when the air cell passage was directed with the swirl or towards the center of the engine, a drop in smoke was observed. However, when it was directed against the swirl of the engine, the air cell had a negative impact. Researchers proposed that, in the former case, the gas jet created a stagnant interference region that hindered the combustion in the "flame clusters" immediately following that region.

Mather and Reitz [9] at the University of Wisconsin-Madison further demonstrated the importance of the location and direction of the mixing in a computational study on the use of air cells in a Caterpillar 3401 test engine. Researchers investigated the four different air cell configurations, each with a different air cell location and connecting passage direction. It was discovered that only one of the four configurations tested yielded a reduction in soot. Researchers concluded that this was indicative of how sensitive this system is to the interplay between the in-cylinder air flow, the fuel spray, and the gas jet.

The oxygen content is also thought to have considerable influence over the effect of the gas jet since oxygen atoms are principle participants in soot oxidation. Yamaura *et al.* [4] demonstrated the importance of this parameter by injecting various gases into the combustion chamber of a naturally aspirated, direct injection diesel engine. Researchers found a large benefit to injecting oxygen as opposed to inert gases such as argon, helium, or nitrogen.

In the current investigation, the authors investigated the affect of both of the aforementioned parameters on DI diesel combustion. Mixing was enhanced in this study using an auxiliary gas injection (AGI). The affect of the direction of that injection was investigated using three different gas injection angles (see Figure 1). At two of these directions, both nitrogen and air were injected to determine the effects of the oxygen concentration of the gas jet.

EXPERIMENTAL SETUP AND PROCEDURE

The engine used in this investigation is a single cylinder, 1.2 liter, direct injection diesel engine with simulated turbocharging. This engine has zero swirl and a 16 to 1 compression ratio. For this study, it was equipped with an auxiliary gas injector, which was used to increase in-cylinder mixing by injecting either air or nitrogen into the combustion chamber. Figure 1 shows the placement of this injector relative to the fuel injector and pressure transducer as well as the three gas injection directions used in this study as seen from a plan view. These three direction (labeled A, B, and C) are aimed 0° , 45° , and 90° from the center of the combustion chamber, respectively.

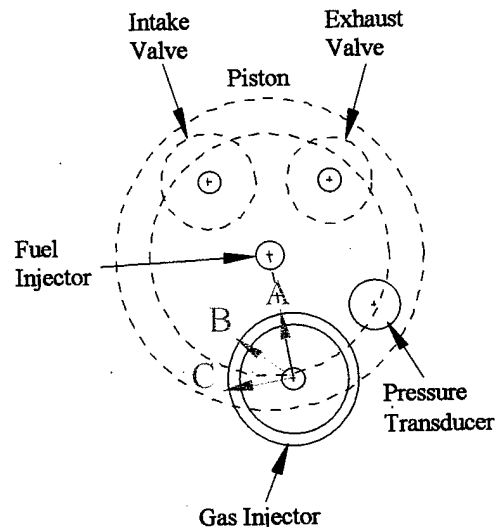


Figure 1. Cylinder Head Configuration and AGI Directions

The fuel injection system on this engine consists of a Robert Bosch Model P-6000 Pump which supplies fuel to a Stanadyne 780328 fuel injector. The nozzle of the injector has eight equally spaced 0.18 mm holes at a 165° cone-angle. The popping pressure for this injector was found to be 22 MPa (3200 psi). This was believed to be the minimum injection pressure for this system, occurring at the beginning and end of the injection event. The fuel injection pressure should be somewhat larger than this value during the bulk of the event.

The gas injector used in this investigation is a Diesel Technologies compressed natural gas injector. This injector is solenoid activated and requires 12 volts/24 amps to energize. The nozzle tip had a single hole, 0.7 mm in diameter oriented 45° downward into the combustion chamber (see Figure 2). This angle was

chosen as an optimum after studying the effect of injection angle on air motion using a KIVA simulation [1].

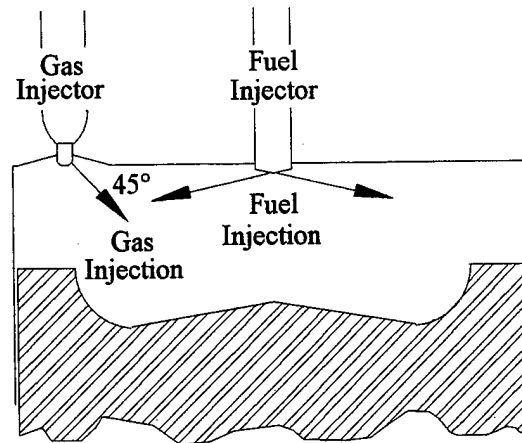


Figure 2. Cross Section View of Combustion Chamber

Gas was injected at 13.8 MPa (2000 psi) throughout this study. The temperature of the gas jet was not controlled; however, it was monitored and found to be 290-305K (62-89°F) at all times. The beginning of gas injection (BOGI) was set at 10 CA ATDC and the duration of gas injection (DOGI) was set at 9.69 ms (87.2 CA at 1500 rpm) for all injection cases run in this study. The BOGI value was set after preliminary testing indicated that injecting at that time yielded the largest soot reduction. DOGI was set at the shortest duration attainable with the current gas injection system.

Five distinct gas injection cases were run in this investigation. These cases differed in gas injection direction and composition. Table 1 shows the directions and compositions of these five cases. As this table indicates, three gas injection directions were examined. All three were tested using nitrogen as the injection specie. To determine the effect of AGI oxygen concentration, air was tested at two of the three AGI directions.

For all five experiments outlined above, the engine was operated at 1500 rpm. Turbocharging was simulated by regulating and heating the intake air to 179 kPa (26 psia) and 60°C (141°F) and adjusting the exhaust pressure to 180 kPa (26.2 psia). Fuel was injected at 2.2 CA BTDC, the most retarded fuel injection timing possible on this engine. This was done to ensure choked flow from the injector, thus forcing the mass flow, momentum, and kinetic energy out of the injector to remain constant throughout the gas injection process. This was also done because the retarded fuel injection timing was thought to represent a case of low NO and poor air utilization.

Table 1. Gas Injection Direction and Composition

	AGI Direction	AGI Composition
Experiment #1	A	Nitrogen
Experiment #2	B	Nitrogen
Experiment #3	C	Nitrogen
Experiment #4	A	Air
Experiment #5	B	Air

Soot measurements were taken using a mini-dilution tunnel. A complete description of the mini-dilution tunnel can be found in a paper by MacDonald *et al.* [10]. Soot samples were captured on a 47 mm diameter filter for approximately 30 minutes. Dilution ratios were determined for each sample by measuring the CO₂ concentrations of both the dilution gas and the raw engine exhaust. Those concentration as well as those of species such as NO and CO was measured using a Nicolet REGA 7000 Real-Time Exhaust Gas Analyzer Fourier Transform Infrared (FT-IR) system. The soluble organic fraction (SOF) of each sample was determined using the Soxhlet extraction method [11] with dichloromethane as the solvent.

COMPUTATIONAL PROGRAM

Multidimensional computer simulations of AGI in the TACOM-Labeco engine were performed to support experimental efforts. Simulations of experiments 4 and 5 were conducted to provide insight into differences in combustion and fluid mechanics between direction A and B cases.

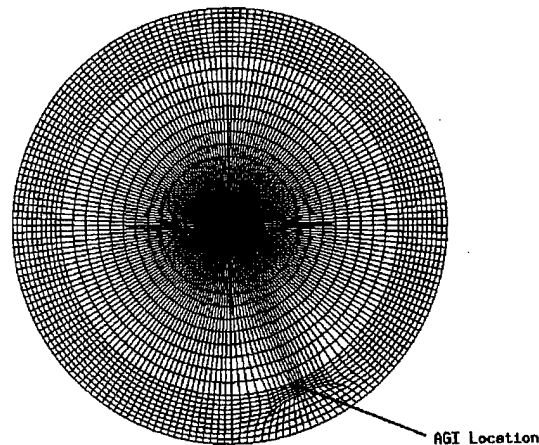


Figure 3. Top View of the Computational Domain.

A modified version of the KIVA code [12] with improved submodels for the diesel spray, combustion, and pollutant formation was employed for these simulations. A description of these submodels can be found in Mather and Reitz [13].

Figure 3 shows the computational domain, a cylindrical grid consisting of 81,000 cells. The gas injector was modeled using a special high-speed gas jet inflow boundary condition, the location of which is shown in Figure 3. A full description of this jet model and its implementation is presented in a paper by Mather and Reitz [14].

RESULTS AND DISCUSSION

GAS INJECTION DIRECTION – Figure 4 shows the soot emissions at various equivalence ratios ranging from 0.35 to 0.55 for the baseline case (i.e. no gas injection) and the three nitrogen injection cases (experiments #1-3). As a reference, the top x-axis on this figure has air-fuel ratio values. This was done only on this figure in order to give the reader a mental template of the conversion between equivalence ratio and air-fuel ratio. The units for soot (and NO) emissions are shown here based on indicated values for power rather the industry standard brake values because the study was conducted on a single cylinder engine, for which torque reading tend to be less stable than in multi-cylinder engines. On this figure, data points represent average soot values at a given equivalence ratio. The lines that accompany these data points are statistical representations of the data along with their upper and lower 95% confidence bands. These lines were generated using a statistical package that extrapolated the lines beyond the range of the data. Caution should be taken however in using those extrapolated values.

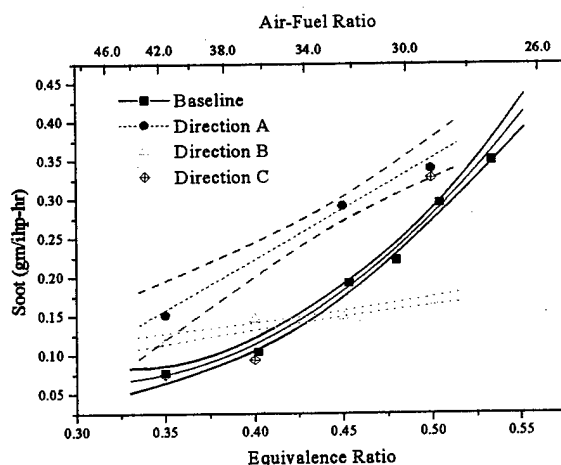


Figure 4. Soot Emissions for Three AGI Directions

Figure 4 indicates that when no gas was injected soot emissions increased with equivalence ratio according to a second order polynomial. This trend is expected when taking into account the fact that soot is related

to the quality of fuel-air mixing and that, as the amount of fuel in the cylinder increases, it becomes exceedingly difficult to adequately mix these two substances. As a result, the increase in soot becomes greater as the equivalence ratio increases.

Of the three gas injection directions used in this study, only direction B yielded a reduction in soot. However, even at this direction, the gas injection only brought about a decrease at high loads. At low loads, the gas jet caused an increase in soot. Injecting in direction A (i.e. straight into the combustion chamber) caused an increase in soot emissions at all equivalence ratios. Injecting in direction C (i.e. 90° from the center of the combustion chamber) appeared to have no affect on soot.

It is believed that theses results can be explained by examining how changes in gas injection direction alter the interaction between the gas jet and the fuel spray. To determine the nature this interaction for each gas injection direction, the trajectories of the eight fuel sprays were superimposed onto the plan view drawing of the combustion chamber (see Figure 5). The sole purpose of this figure is to determine where and how the gas jet collides with the various spray plumes. Consequently, the superimposed images shown here are not on the same scale. In addition, since it is beyond the scope of this study, no in depth comparisons of the gas jet and fuel spray momentums and collision velocities is presented here. It should be noted, however, that the momentum fluxes of the two injection events were the same order of magnitude which would enable each of them to exert influence over the other.

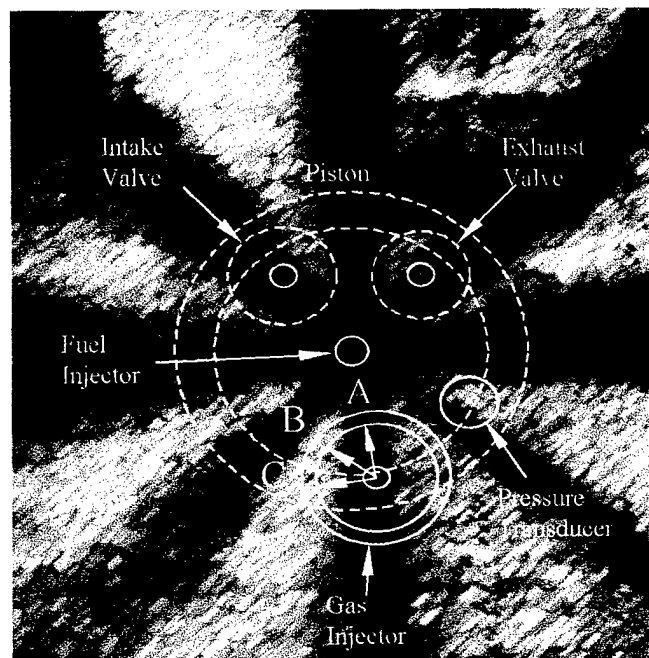


Figure 5. Fuel Spray-Gas Jet Interaction

From this figure, it appears that when direction A was used the jet worked directly against the motion of the fuel spray. It is believed that this interaction prevented the fuel spray from penetrating as far into the combustion chamber as it would have if no gas jet was present. As a result, combustion in the effected plume was richer, thus causing an increase in soot emissions. Additionally, the area of increased turbulence was at the head of the fuel spray in this case, an area that was shown to have little air entrainment by both Won *et al.* [15] and Dec [16]. As a result, the benefit of increasing in-cylinder mixing was minimal.

When gas was injected in direction B, the gas jet appeared to crash into the adjacent fuel spray in an area where Won *et al.* [15] and Dec [16] claimed that the bulk of air entrainment occurs. As a result, the gas jet was able to increase air entrainment and fuel-air mixing in this case, thus explaining the decrease in soot emissions. The fact that an increase in soot emissions was observed at the low loads indicates that an additional mechanism is present which either enhances soot formation or inhibits soot oxidation. The most plausible mechanism comes from the fact that an inert gas was injected. As a result, the average oxygen concentration of the gas being entrained in the fuel spray was reduced, thus reducing the oxygen concentration where soot chemistry takes place [15, 16]. At high loads, the benefits of the mixing were enough to overcome this effect; however, at low loads where mixing was not as much of an issue, this effect had a dominating impact.

When gas was injected in direction C, the gas jet appears to hit the cylinder wall before reaching a fuel spray. As a result, the gas jet velocity was far less when it reached an area where it could have an impact due to either premature dissipation or increased travel distance, causing it to have little impact on soot emissions.

Computational results support the proposed differences between injecting in direction A and direction B. Figures 6 and 7 show snapshots at 20 CA ATDC of how gas injection affects the fuel spray and the soot clouds for these two directions, respectively. In Figure 6, the fuel spray facing the gas jet has been shortened and that the area of the soot cloud is larger and closer to the center of the combustion chamber. However, in Figure 7 no such shortening of the fuel spray was observed. In addition, when injected in direction B the gas jet sweeps aside the soot cloud immediately in front of it and proceeds towards the side of the adjacent fuel spray.

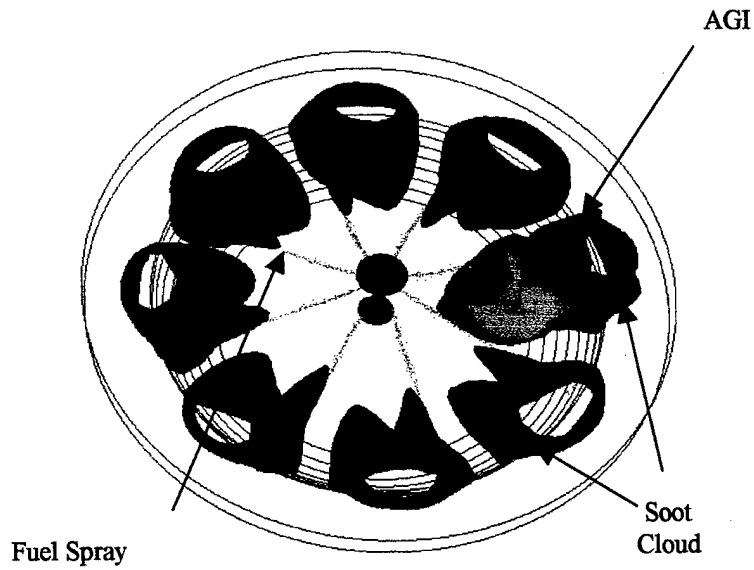


Figure 6. AGI in Direction A (20 CA ATDC)

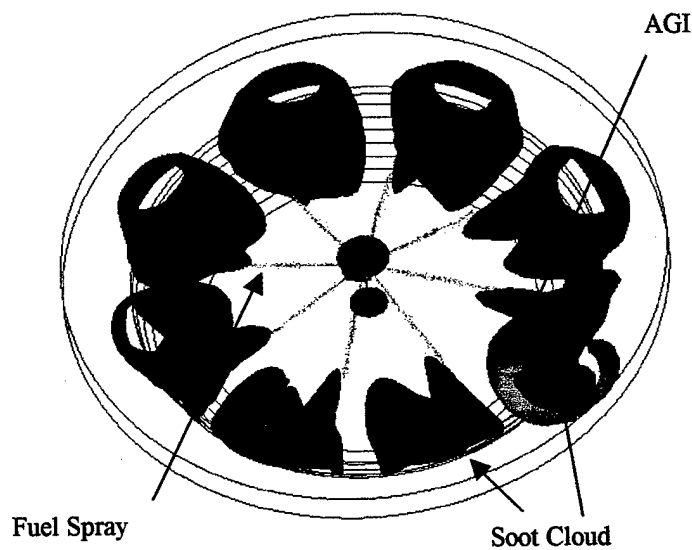


Figure 7. AGI in Direction B (20 CA ATDC)

The computational results offer an additional explanation for the differences between these two injection direction cases. As combustion proceeds, the gas jet in the direction A case flows directly across the combustion chamber only affecting one or two additional soot clouds (see Figure 8). However, when injected in direction B, the gas jet swirls around the combustion chamber affecting all but three soot clouds that remain at 98 CA ATDC (see Figure 9).

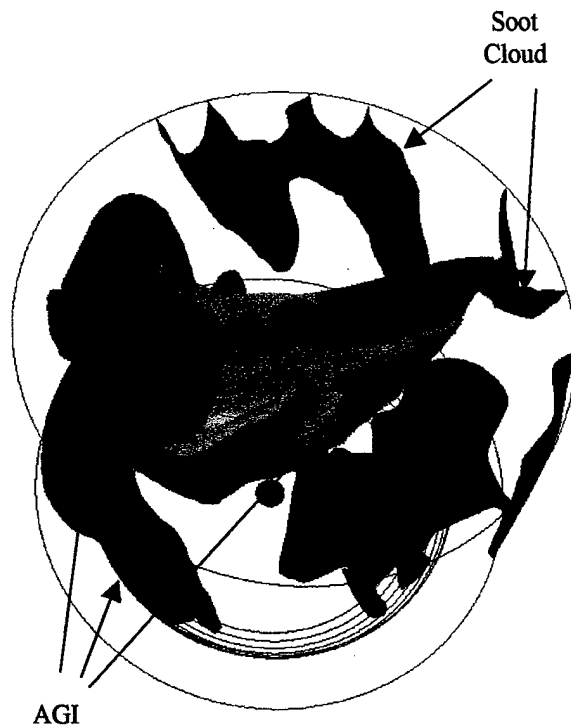


Figure 8. AGI in Direction A (98 CA ATDC)

Despite the various changes in soot, SOF percentages did not change significantly from baseline SOF values for any of the cases discussed here. This indicates that the mechanisms that cause the changes in soot here do not affect the deposition of hydrocarbons on soot particles.

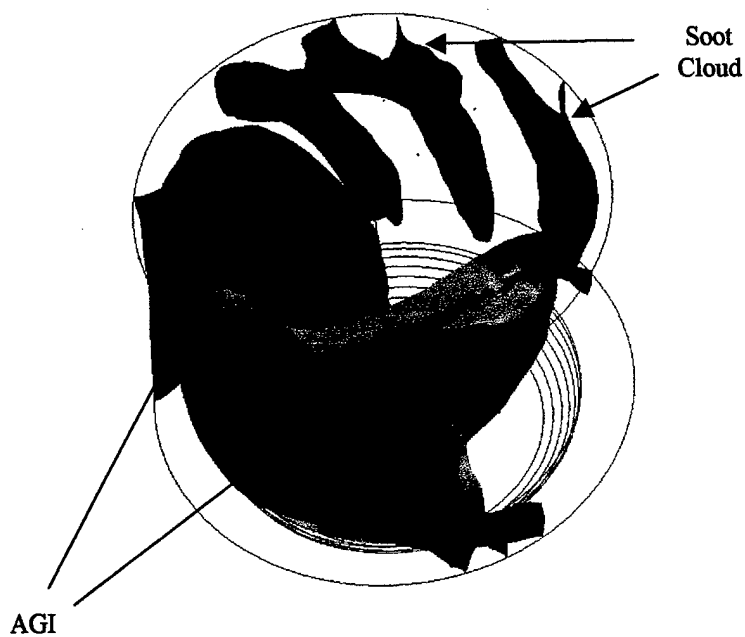


Figure 9. AGI in Direction B (98 CA ATDC)

Figure 10 shows the NO emissions for the various nitrogen injection cases discussed above. For all three injection directions, a decrease in NO emission was observed. This difference was primarily due to an increase in power output. On average, injecting in either of those directions yielded a 2-3% increase in power. When plotted on a gram per kilogram of fuel basis, the difference in between baseline NO and that for the gas injection almost completely disappears (see Figure 11).

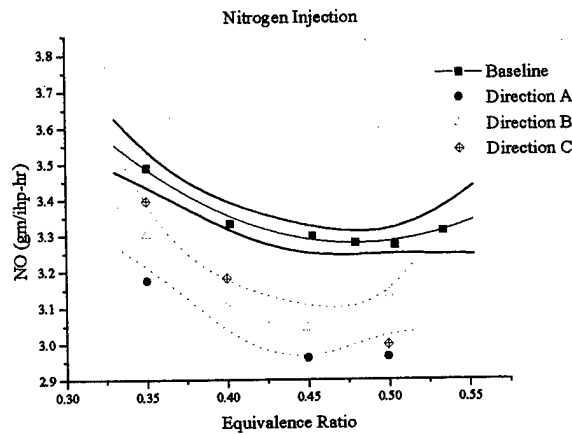


Figure 10. NO Emissions for the Various Gas Injection Direction Cases (gm/ihp-hr).

It can be seen from Figures 5 and 6 that the drop in NO emissions was more substantial for the case where gas was injected in direction A. It is believed that this drop in NO was a result of the fact that, as explained earlier, the gas jet impeded the progress of the fuel spray, causing locally rich combustion and lower combustion temperatures.

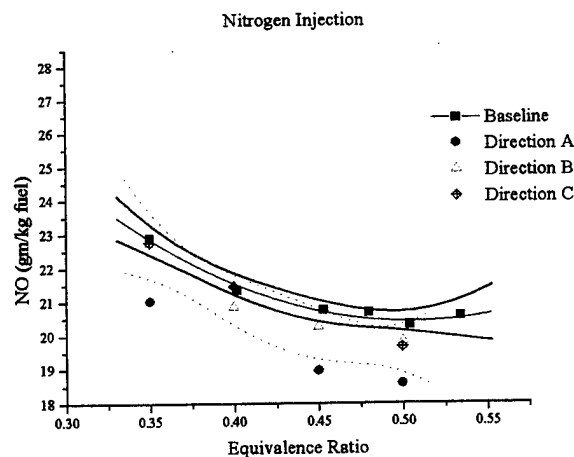


Figure 11. NO Emissions for the Various Gas Injection Direction Cases (gm/kg fuel).

OXYGEN CONCENTRATION – As discussed in the previous section, injecting nitrogen in direction B was found to have a detrimental effect on soot at low loads. It was suspected that the mechanism behind this increase was chemical in nature, rather than a product of the mixing. This notion seems to be well founded since this detrimental effect disappeared when air, rather than nitrogen, was injected (see Figure 12). A similar drop in soot was observed at high loads between air and nitrogen injection cases, thus suggesting that this detrimental effect was present at all loads when nitrogen was injected and that at high loads it was overcome by the effects of enhanced mixing.

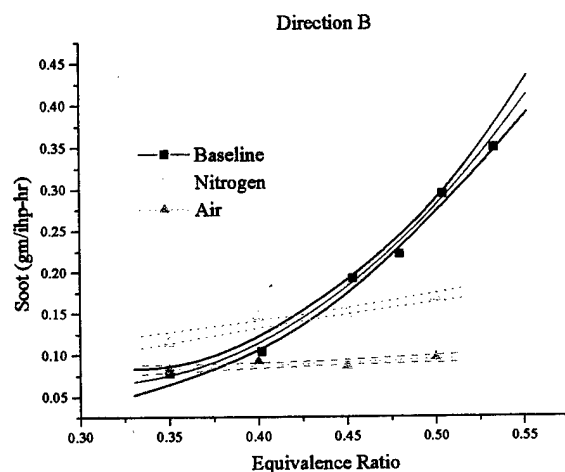


Figure 12. Soot Emissions for Direction B.

The benefits of using air was also observed when direction A was used, although the benefits were not as pronounced (see Figure 13). Despite this fact, injecting air in this direction still yielded an increase in soot. For this reason, it is believed that the main effect in this system is that of the obstruction of the fuel spray by the gas jet. The benefit of using air is most likely due to the fact that, as the injected gas moves around the fuel spray it is eventually entrained. Therefore, the presence of oxygen in the injected gas would be beneficial.

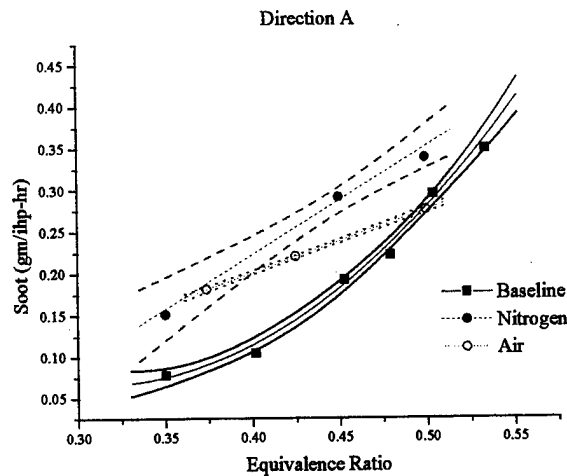


Figure 13. Soot Emissions for Direction A.

The oxygen concentration of the gas jet also affects NO emissions. Figures 14 and 15 show the NO results (in gm/ihp-hr and gm/kg fuel, respectively) comparing the effects of air and nitrogen injection when the gas was injected in direction A. Figures 16 and 17 were the NO results on those same basis for the direction B injection cases. As was discovered, NO emissions appeared to be much lower than baseline emissions, except when air was injected in direction B, when shown on a gm/ihp-hr basis. When presented in gm/kg fuel, the difference between the baseline gas injection cases diminishes.

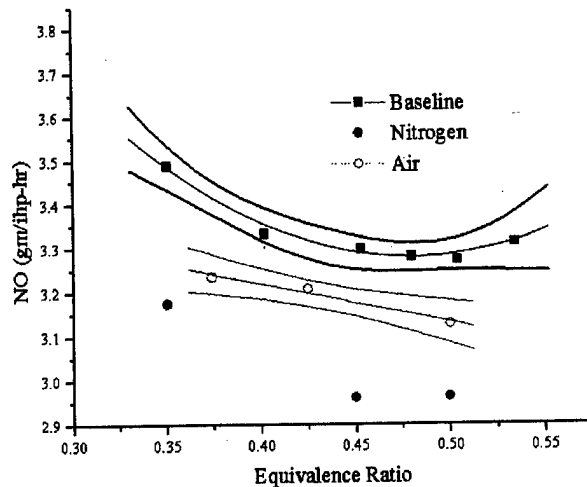


Figure 14. NO Emissions (gm/ihp-hr) for Direction A.

Using Figures 15 and 17, one can see that air caused an increase in NO from baseline NO emissions for both gas injection directions. However, this increase was much smaller when the gas was injected in direction A rather than direction B. This is consistent with the hypothesis discussed earlier explaining the

difference in NO results for the nitrogen injection cases at these two injection directions. Nonetheless, regardless of the units of NO emissions, air appears to cause an increase in NO when compared to the nitrogen injection. This indicates that there is a chemical effect when nitrogen is added to the cylinder that suppresses NO formation in both injection direction cases.

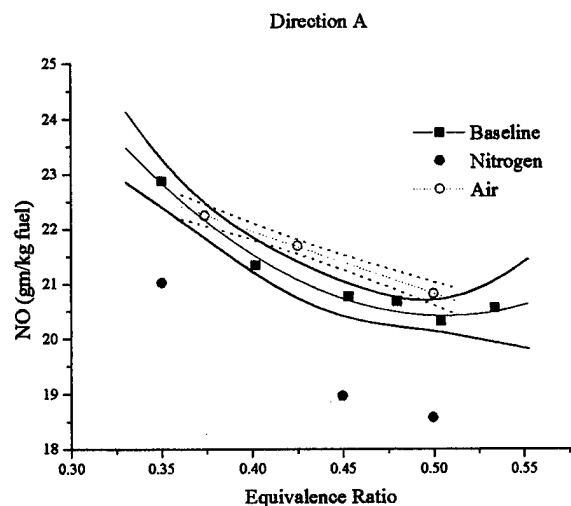


Figure 15. NO Emissions (gm/kg fuel) for Direction A.

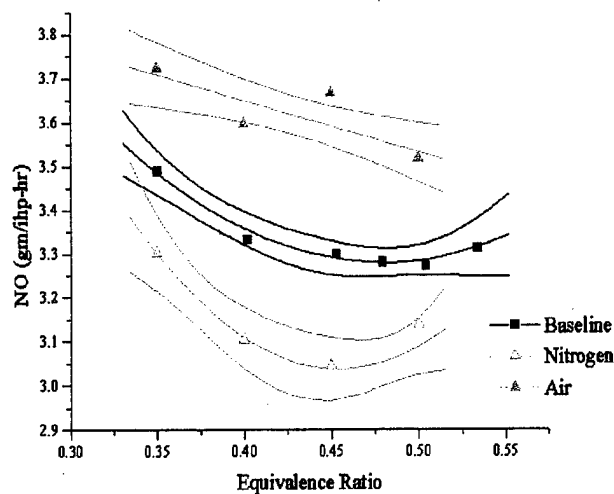


Figure 16. NO Emissions (gm/ihp-hr) for Direction B.

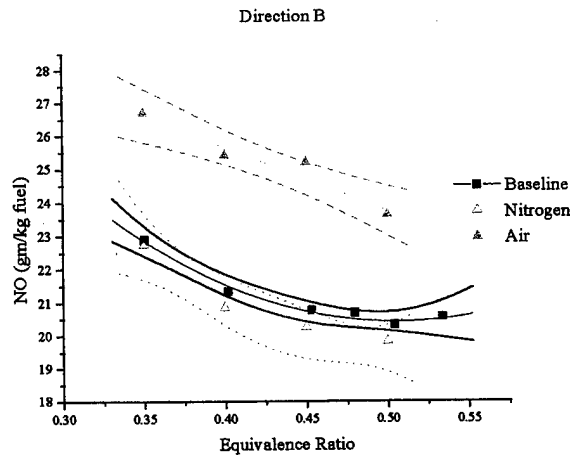


Figure 17. NO Emissions (gm/kg fuel) for Direction B.

SOOT-NO_x TRADEOFF - Figure 18 illustrates how each case compares to the soot-NO_x tradeoff for the engine used in this study at $\Phi=0.50$. It is clear that, if the gas injection is set up correctly (direction B) and used in conjunction with a point of low NO emissions tremendous gains can be made beyond the usual tradeoff curve.

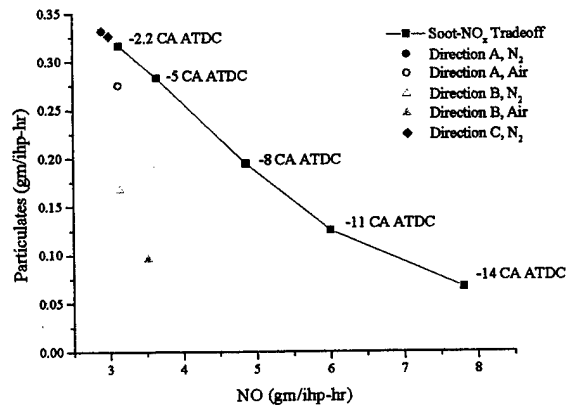


Figure 18. Comparison of AGI Results with the Soot-NO_x Tradeoff

SUMMARY AND CONCLUSIONS

The purpose of this investigation was to determine what influence gas injection direction and oxygen concentration have on emissions when some form of gas jet intrusion is used to enhance in-cylinder mixing. Three different gas injection directions and two different gas injection compositions were examined. The results of the study are summarized below.

1. Gas injection direction had a profound influence on the effect of AGI. This is thought to be a result of changes in the fuel spray-gas jet interaction.
 - Injecting directly at the fuel spray (direction A) impedes the progress of the spray, thus causing an increase in soot. It also appears to affect fewer soot clouds.
 - Injecting at the side of a fuel spray (direction B) in an area of high air entrainment causes a decrease in soot emissions by increasing soot oxidation rates. It also sweeps through most of the soot clouds.
 - Injecting towards the cylinder wall (direction C) has little effect on soot emissions because of a decrease in gas jet velocity with increased dissipation and travel distance.
2. SOF percent is completely unaffected by the injection of gas.
3. Injecting an inert gas reduces the oxygen concentration surrounding the combustion, which suppresses soot oxidation or enhances soot formation, thus causing an increase in soot emissions.
4. When air is injected, the aforementioned detrimental effect on soot disappears; however, this causes an increase in NO emissions.

The results of this study show that gas injection can have detrimental effects on soot when done improperly. However, when done properly it is a very effective way to overcome the usual soot-NO_x tradeoff.

REFERENCES

1. Kurtz, E.M. and Foster, D.E., "Exploring the Limits of Improving DI Diesel Emissions by Increasing In-Cylinder Mixing", SAE 982677.
2. Kamimoto, Takeyuki, Suichi Osako, and Shin Matsuoka, "An Air Cell DI Engine and Its Soot Emission Characteristics", SAE 831297.
3. Kamimoto, Takeyuki, Suichi Osako, and Shin Matsuoka, "An Air Cell DI Diesel Engine and Its Soot Emission Characteristics", JSME Journal Series B Vol. 50 No. 453 pp1363-1371 (May 1984). (in Japanese)
4. Kamimoto, Takeyuki, Shuichi Osako, Shin Matsuoka, "A Study for Reducing Diesel Exhaust Emission by Gas Injection (1st Report: Reduction of Black Smoke by Combustible Gas Injection)", 8th *International Combustion Engine Symposium*, Japan, 123, p.129-134, 1990. (in Japanese)
5. Golding, L., "The Effects of Augmented Mixing on Diesel Combustion", M.S. Thesis, Mechanical Engineering Department, University of Wisconsin-Madison, 1992.
6. Murayama, T., T. Chikahisa, K. Yamane, and M. Xu, "Reduction of Smoke and NO_x Emissions by Active Turbulence Generated in the Late Combustion Stage in D.I. Diesel Engines", *Proc. 18th Symp. Int. Con. Combust. Eng.*, D132, p1129-1141, 1989.
7. Konno, Mitsuru, Takemi Chikahisa, and Tadashi Murayama, "Reduction of Smoke and NO_x by Strong Turbulence Generated During the Combustion Process in D.I. Diesel Engines", SAE 920467.

8. Choi, C.Y., and D.E. Foster, "In Cylinder Augmented Mixing Through Controlled Gaseous Jet Injection", SAE 952358.
9. Mather, D.K. and Reitz, R.D., "Modeling the Use of Air-Injection for Emissions Reduction in a Direct-Injected Diesel Engine", SAE 952359.
10. MacDonald J., S. Plee, J. D'Arcy, and R. Streck, "Experimental Measurement of the Independent Effects of Dilution Ratio and Filter Temperature on Diesel Exhaust Particulate Samples", SAE 800185.
11. Newkirk, Matthew S., "Application Methods for Determining Total Organic Contribution to Diesel Particulates", ASME Paper 92-ICE-16.
12. Amsden, A.A., *KIVA-3V: A Block-Structured KIVA Program for Engines with Vertical or Canted Valves*, Technical Report LA-13313-MS, Los Alamos National Labs., 1997.
13. Mather, D.K. and R.D. Reitz, "Modeling the Influence of Fuel Injection Parameters on Diesel Engine Emissions", SAE 980789.
14. Mather, D.K. and R.D. Reitz, "Modeling the Effects of Auxiliary Gas Injection on Diesel Engine Combustion and Emissions", SAE 200-01-0657.
15. Won, Young-Ho, Takeyuki Kamimoto, and Hidenori Kosaka, "A study on Soot Formation in Unsteady Spray Flames via 2-D Soot Imaging", SAE 920114.
16. Dec, John E., "A Conceptual Model of DI Diesel Combustion Based on Laser-Sheet Imaging", SAE 970873.

Effects of Oxygen Enhancement on the Emissions from a DI Diesel via Manipulation of Fuels and Combustion Chamber Gas Composition

Brief Summary

Technologies are now becoming available in which the ratio of oxygen to nitrogen in the inlet air stream can be varied. Technologies such as polymer membrane separation and pressure swing absorption for altering the ratio of O_2 to N_2 in the intake air may be commercially viable for adaptation to internal combustion engines. To this end, oxygen enhancement in a direct injection (DI) diesel engine was studied to investigate the potential for particulate matter and NO_x emissions control and hence its potential for allowing increased power density. The local oxygen concentration within the fuel plume was modified by oxygen enrichment of the intake air and by oxygenating the base fuel with 20% methyl t-butyl ether (MTBE). The study collected overall engine performance and engine-out emissions data as well as in-cylinder two-color measurements at 25% and 75% loads over a range of injection timings. The study found oxygen enhancement, whether it be from intake air enrichment or via oxygenated fuels, reduces particulate matter, the effectiveness depending on the local concentration of oxygen in the fuel plume. Since NO_x emissions depend strongly on the temperature and oxygen concentration throughout the bulk cylinder gas,

the global thermal and dilution effects from oxygen enrichment were greater than that from operation on oxygenated fuel. There is no doubt that oxygen enrichment can be used for increasing the power density, for a given smoke limit constraint.

INTRODUCTION

More complete burning, faster burn rates, and the ability to burn more fuel can occur with increases in the oxygen concentration of a fuel-air mixture, often beneficially increasing the efficiency and power output of an engine and reducing the emissions of most exhaust pollutants (e.g., smoke, particulate matter, and THC) [9]. However, the increased oxygen concentration has a detrimental thermal and dilution effect on NO_x emissions, although engine fuel timing optimization may minimize these effects.

Oxygen enhancement has typically been achieved through oxygenated fuels and has shown promise [1-7]. A number of lab studies have also been conducted on oxygen enrichment of the intake air [8-10]. The practical viability of oxygen enrichment for a mobile diesel depends on the availability of a simple, compact system that will extract oxygen economically from the air. Up until recently, none of the methods for non-cryogenic oxygen separation from atmospheric air (e.g., membrane diffusion, molecular sieves, and oxygen absorption) were sufficiently advanced or perfected for practical application. However, now scientists at Argonne National Laboratory with chemists at Compact Membrane Systems have developed a membrane that efficiently separates regular air into oxygen and nitrogen [11].

Miyamoto et al. [1] conducted a study of biodiesel oxygenate fuels and has shown that the improvement in the exhaust emissions and the thermal efficiency depended almost entirely on the oxygen content in the fuels, regardless of the oxygenate to diesel fuel blend ratios or type of oxygenate. Similarly, this paper will investigate oxygen enhancement through oxygen enrichment and use of an oxygenated fuel to compare and contrast the effects each method has on the performance and emissions from a turbo-charged DI diesel.

EXPERIMENTAL DESCRIPTION

OPTICAL-ACCESS ENGINE

As specified in Table 1, the optical accessible engine used in this investigation is a Cummins, single-cylinder, direct-injection, 4-cycle diesel, adapted from an in-line six-cylinder Cummins N14-series engine. The N14 engine's low swirl, turbo-charged, 4 valve, centrally located direct-injection combustion system is representative of modern heavy-duty diesels used today. A top of the line N14 (a series N14-500E) develops 373 kW (500 hp) at a governed speed of 2100 rpm. Torque ratings are 2375 N-m (1750 ft-lbf) and 2239 N-m (1650 ft-lbf) at 2100 and 1200 rpm, respectively. Depending on the Cummins N14 engine model, advertised power can range from 246 kW (330 hp) to 391 kW (525 hp) and torque from 1830 N-m

(1350 ft-lbf) to 2508 N-m (1850 ft-lbf). For the single-cylinder engine used in this study, power output peaked at values of 40 kW (54 hp) and 30 kW (40 hp) at 1500 and 1200 rpm, respectively, corresponding to torque ratings of 252 N-m (186 ft-lbf) and 244 N-m (180 ft-lbf), respectively.

TABLE 1: ENGINE SPECIFICATIONS

Engine Type	Cummins N14 Single Cylinder Diesel
Cycle	4-stroke
Combustion Chamber	Quiescent
Piston Chamber	Shallow Dish
Number of intake valves	2
Number of exhaust valves	2 ^a
Compression Ratio	13.1:1
Swirl Ratio	1.4
Displacement	2336 cc
Bore	139.7 mm
Stroke	152.4 mm
Combustion chamber diameter	97.8 mm
Connecting rod length	304.8 mm
Piston pin offset	None
Injection System	Unit Injector, Direct Injection (DI)
Nozzle Dimension	8 × Φ 0.200 mm
Length/diameter of holes (l/d)	4.1
Spray Angle	152°

^a Two identical production N14 cylinder heads were used in this study. One head was made optically accessible by replacing one of its two exhaust valves with a sapphire window.

In 1994, hardware improvements were made to the N14 engine, including changes in the pistons, air handling system, and cooling system. The new pistons are two-piece articulated units with forged steel crowns, higher top rings and aluminum skirts. The piston geometry was re-designed to promote improved swirl and combustion. The single-cylinder engine used in this study does not incorporate the new articulated piston. In this study, the piston has a scalloped design and is rated for a 15:1 compression ratio engine. The actual compression ratio, however, is 13.1:1 due to modifications to the head to allow optical access. For the air handling system, the N14 now has a new cast iron alloy cylinder head with a flat combustion face (non-scalloped head), wider valve bridges and newly designed ports, valves and valve seat inserts. Swirl intake ports are designed to optimize air mixing within the cylinder to promote lowered emissions. The new valves and valve seat inserts are intended to improve fuel consumption and head durability. As with the old design, each cylinder in the N14 engine has two intake and two exhaust valves for providing high volumetric efficiency and good exhaust scavenging. Push-tubes, injector cam followers and rocker levers also now include a ball and socket geometry to decrease wear. A new camshaft in the N14 engine is designed for higher lift, increased injection pressure (above 155 MPa), and higher durability through micro-finished lobes.

The single-cylinder lab engine used in this study does not include any auxiliary systems. Therefore, changes made to the commercial N14 engine for auxiliary systems (such as the turbocharger and cooling system) were simulated by lab equipment.

Two production N14 cylinder heads were used in this study, one unmodified and employed in emissions and performance studies, the other modified to enable combustion visualization studies (i.e., two-color analysis). Both heads were machined to incorporate a pressure transducer port. The head used for the combustion visualization studies had one of its two exhaust valves removed to provide an access port to the cylinder. A sapphire window is placed in the optical access port for visualization of the spray plums, as can be seen from Fig. 1. To make this access port, the 3-valve head was bored out at the location of the absent exhaust valve and a bushing was pressed into the hole to seal off the coolant and fuel passages. When this 3-valve head is being used, the one remaining exhaust valve has to be actuated by an extended rocker lever. Normally, the two exhaust valves are opened simultaneously when the rocker arm pushes down a crosshead piece located above the two valves. Care was taken to ensure valve timing and lift is similar to the unmodified rocker assembly.

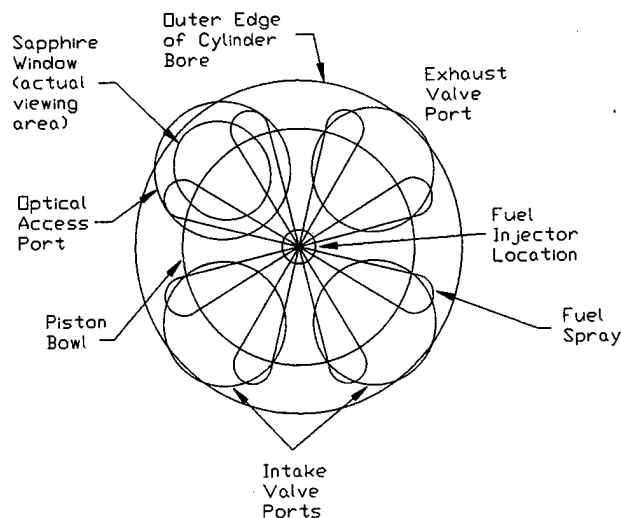


Figure 1. Plan view of modified cylinder head. Optical viewing area is at location of missing exhaust valve. As a scale, Bore = 139.7 mm (5.5 in). As drawn, the distance along the inner periphery of the fuel jet to the sapphire window is 27 mm.

A blow-by valve was added to the rocker-arm housing to help in monitoring the status of the engine. Tests under warm, simulated turbo-charged engine conditions (at 1500 rpm and $\phi=0.3$, or medium single cylinder torque of 186 N-m) indicated 1.5% of the intake charge ended up as blow-by exhaust. The blow-by was considered small and acceptable (i.e., ring pack, valves, etc. were all considered in proper operation). Bellows meters measured this blow-by. To simplify the monitoring of the engine blow-by, the Bellows

meters were replaced with a manometer. Deviations in manometer readings of the blow-by from typically recorded values indicated transient or unhealthy engine operation.

Besides the differences mentioned above between the single-cylinder and commercial engine, the single-cylinder engine needs to be connected to a balancing box (with counter-rotating balancing weights) and mounted on a spring-mounted isolation pad to reduce vibrations. Since the engine does not include any production auxiliary systems, fuel metering and intake air are provided by laboratory auxiliary systems. Coolant is also provided by an external system consisting of a pump and an atmospheric cooling tower. The coolant is a 50/50 mixture of antifreeze and distilled water. Turbo-charging is simulated using high-pressure dehumidified and filtered house air, along with an air heater. The engine was motored and its speed controlled, to within 2 rpm, by a 225 hp dynamometer. The controller allows only steady-state tests.

FUEL SYSTEM

The Cummins N14 engine uses the electronically controlled Celect injector. On the top of the injector is a solenoid valve used to control the amount of fuel and the injection timing upon command from the engine's Electronic Control Module (ECM). For the single-cylinder engine used in this study, the ECM was bypassed and a personal computer equipped with a software-based controller was used to control the injector. The electronically controlled Celect injector uses camshaft actuation to build injection pressures (just like the Cummins PTD injector), but it has a closed nozzle and a two-piece plunger, rather than the open nozzle and one-piece plunger of the PTD injector.

The upward movement of the timing plunger controls fuel metering when the normally open solenoid valve is closed. The solenoid valve opens upon deactivation of the solenoid signal. The timing of the solenoid deactivation occurs at timing-valve-opening (TVO). TVO signals the end of fuel metering. The downward movement of the timing plunger and the closing of the solenoid valve control the start-of-injection. The solenoid control valve closes upon receiving an electronic timing-valve-close (TVC) signal. With the solenoid valve closed, pressure builds in the metering chamber as the timing plunger compresses the trapped diesel fuel. At a preset pressure the needle lifts and injection starts. The TVC timing would be the start-of-injection (SOI) if the fuel injection system did not have any mechanical or electronic delays (such as the mechanical compressibility of diesel fuel and stiffness of injector spring). Injection ends when the pressure is less than the preset pressure and the needle is seated. The Celect injector enables the fueling and the injection timing to be varied independently of each other by choice of TVO and TVC timings, respectively. Higher fueling rates are obtained by retarding the TVO signal since the timing plunger will have risen to allow a larger volume in the metering chamber.

The injection timing was monitored with a strain gage on the fuel injector's push rod. The strain gage and push rod assembly was provided, along with timing data taken from a Cummins M11 engine, by Cummins. The M11 timing data was obtained under an identical injection system configuration (i.e., same strain gage assembly and same fuel injector) to that found in the N14, with the exception of a needle-lift indicator fitted into the M11's fuel injector for the more reliable indication of start- and end-of-injection timing. The M11 data was used to help in deciphering the strain signal to determine the true injection timing for the N14 engine.

OXYGEN ENRICHMENT LAYOUT

Modification to the intake system was required for the oxygen enrichment study, as shown in Fig. 2. Oxygen was supplied from eight oxygen tanks pigtailed together in series. The oxygen flows from the oxygen tanks through a pressure regulator, a metering valve, a flowmeter, across the room in oxygen-clean and compatible copper tubing to a back-flow check valve, and then into the intake manifold before the air heaters. The oxygen-enriched air is then heated as required. Since the heaters are before the intake surge tank, the surge tank not only dampens the pressure fluctuations associated with single cylinder engine operation, but also thoroughly mixes the oxygen-air mixture.

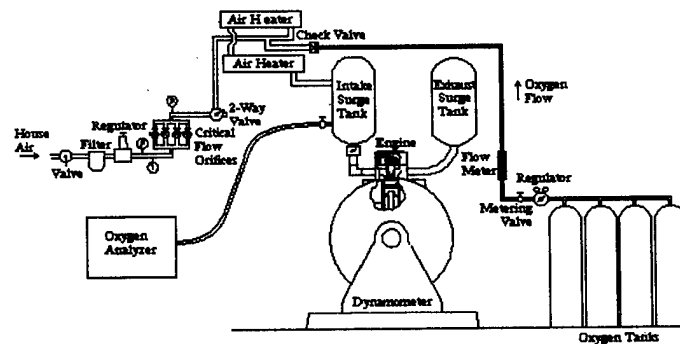


Figure 2. Schematic of lab layout for oxygen-enrichment study. Breakaway view of engine shown.

The oxygen flow rate was calculated, for a given operating condition (i.e., airflow rate), to estimate the desired percent enrichment. A Beckman model OM11-EA oxygen analyzer sampled the intake surge tank oxygen-air mixture for verification of the enrichment rate. If the enrichment rate was not correct, adjustments were made to the pressure regulator and metering valve.

DATA ACQUISITION SYSTEM

Engine pressure and control system timing data was collected on a Power and Energy International (PEI) data acquisition system for both steady state and two-color combustion filming operation. The data acquisition system is based on a personal computer equipped with a PEI DAB-504 data acquisition board.

The board is multiplexed to sample up to four channels. Normally, three channels of data are sampled at increments of 0.25 crank angle degrees, as mandated by the shaft-encoder, and 120 consecutive cycles are stored. For all steady-state data, the 120 engine cycles were ensemble-averaged. The collected pressure data was smoothed with a Fourier series high-frequency-reject-filtering algorithm and post-processed by the ERC's heat release code to obtain heat release rates and combustion data.

High-speed films of the combustion events were used to acquire two-color data. When filming the combustion events, five calibrated halogen bulbs are positioned around the optical access tube so that both the combustion event and the bulbs are imaged together on the film, as shown in Fig. 3. After processing the film and getting the negatives, each film frame is digitized twice with a CCD camera--once for each of two different wavelengths by placing different filters between the film negative and the CCD camera. Fig. 4 schematically shows the digitizing setup.

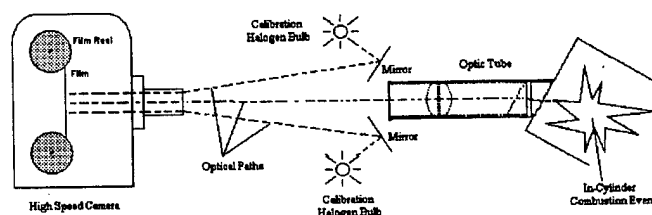


Figure 3. High speed filming setup used to obtain combustion image.

The two filtered, digitized negative images collected for each film frame are then "negated" with the CCD's digital imaging system to make filtered, digitized positive images. These filtered, digitized positive images are then exported as "16 bit raw Intel" files to be imported into the two-color program. The two-color program processes the images to obtain both a temperature and a KL-factor for each pixel of each film frame. Once all film frames are processed for a combustion event, a temporally resolved, two-dimensional field of temperature and KL-factor are obtained.

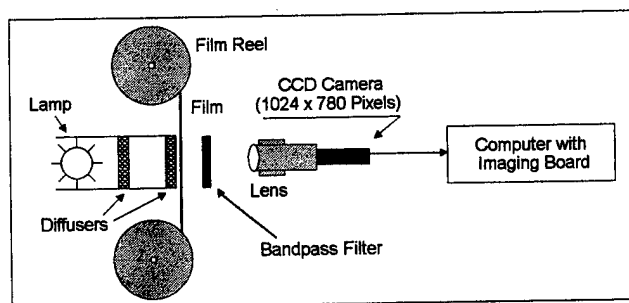


Figure 4. Digitizing Setup used to obtain images at two different wavelengths

Much of the two-color data presented will be "view-averaged." For view-averaged data, all pixels on a film frame that are within the filmed combustion event are averaged together for both a mean temperature and mean KL-factor.

TABLE 2: HIGH LOAD OPERATING CONDITIONS

Engine Load	75%	Mode 6 of CARB 8
Engine Speed	1200 rpm	Peak Torque Speed
Injection Timings	TVC: 10°, 15°, 18°, 25°, 30° BTDC	
Fuel Delivery	185 mg/st	~ 0.65 equiv. ratio
Intake Pressure	26psia	To simulate turbo-charger
Exhaust Pressure	12psig	
Intake Temperature	45 °C	To simulate air-to-air after-cooler
Coolant Temperature	80~83 °C	To stabilize cyl. liner wall temperature
Oil Temperature	85~88 °C	To stabilize piston and head temps
Fuel Temperature	65 °C	To stabilize fuel

OPERATING CONDITIONS AND FUELS

Steady-state operation at 75% load (mode 6 of the CARB 8-mode transient test cycle) was used for the baseline, oxygenate alternative fuel, and oxygen enrichment studies. Oxygen enrichment was also run at a characterized 25% load condition [12]. Tables 2 and 3 summarize the operating parameters under the 75% and 25% loads, respectively.

TABLE 3: LOW LOAD OPERATING CONDITION

Engine Load	25%	Low Load, NA
Engine Speed	1200 rpm	Peak Torque Speed
Injection Timing	11.5° btdc	TVC = 25
Fuel Delivery	53 mg/st	~ 0.25 equivalence ratio
Intake Pressure	24 psia	To simulate NA TDC motored pressure of 5Mpa for a N14 engine with a 16.1 CR
Exhaust Pressure	7.8 psig	Required to get soot Dec et al. [12] ran with 0 psig
Intake Temperature	157 °C	To simulate NA TDC motored temp of 1000K
Coolant Temperature	80~83 °C	To stabilize cylinder liner wall temperature
Oil Temperature	85~88 °C	To stabilize piston and head temperature
Fuel Temp	65 °C	To stabilize the fuel

Since the in-cylinder temperature and soot data were obtained from the post processing of combustion events recorded on negative color film, each filming condition took several weeks to develop and analyze. Therefore, two-dimensional two-color filming was only performed at 75% load for baseline, oxygenated fuel, and oxygen enrichment test operations at the judiciously chosen TVC timings of 10, 18, and 30. The low load operating condition was also filmed at the TVC=25 timing specified in Table 3.

TABLE 4: FUEL PROPERTIES

Name	Fuel Formulation		
Base	$C_{15}H_{27.66}$		
MTBE-Base	Base 80% + MTBE 20% + CI 2500 ppm		
Property		Base	MTBE-Base
Density	(kg/m ³)	846.5	827.4
CN		46.6	46.8
Viscosity ~35°C	(mm ² /s)	2.92	0.9696
Vapor Pressure	(kPa)	1.0	20.0
Calorific Value	(kJ/kg)	42936	42079
IBP	(°C)	192.2	57.1
T10	(°C)	229.4	61.9
T50	(°C)	265.5	256.0
T90	(°C)	308.9	305.1
EP	(°C)	336.7	335.2
Saturates	Vol (%)	67.4	54.0
Aromatics	Vol (%)	29.9	23.9
Olefins	Vol (%)	2.7	2.1
Sulfur Content	Vol (%)	0.0165	0.0132

Two different fuels were used in this study: 1) a base diesel fuel, and 2) an oxygenated alternative fuel. Fuel properties for the fuels are tabulated in Table 4. The oxygenated alternative fuel was composed of 20% methyl t-butyl ether (MTBE), the rest being mostly composed of the baseline diesel fuel, with a small addition of cetane improver (CI). Although the oxygenate alternative fuel study is focused on the effect of the added oxygen in the fuel, the fuel properties shown in Table 4 (and their confounding effects) need to be considered for a fair assessment.

Fuel cetane number will affect ignition delay (as will engine operating conditions), which will in turn have an effect on combustion through changes in both the premixed and mixing controlled burning modes. In general, longer ignition delays lead to larger premixed burning (and less mixing controlled burning). As can be seen in Table 4, the fuel cetane numbers agree quite well between the MTBE blended and base diesel fuels. Results are confounded when fuels with different volatility are compared since a fuel's volatility effects the rate and height of rise of the premixed burning spike. Similarities in volatility between the base diesel and MTBE blended fuels can be seen in Fig. 5. As might be expected, the distillation curves show the MTBE blended fuels are comprised of a much higher volatile fraction, nearly 20% by volume. As the lower boiling point temperature components vaporize, the MTBE blended fuels begin to more closely resemble the volatility of their base component fuel.

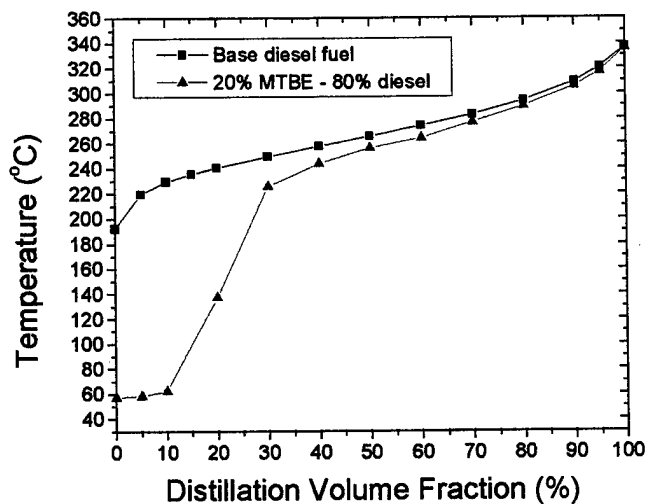


Figure 5. Distillation curves of test fuels.

Research by Muller [13] has indicated that a 50 °C increase in initial boiling point can produce a 5 percent increase in exhaust nitrogen oxide emissions. Other researchers have also found increasing volatility increases nitrogen oxide emissions [14]. However, more recent studies have not found any clear volatility effect [15, 16]. Special attention is warranted since the initial boiling points are as much as 130 °C different between the fuels. Applying Muller's conclusions, this initial boiling point difference may result in a 13 percent decrease in exhaust nitrogen oxide emissions for the MTBE blended fuel mixture compared to the baseline fuel. However, the higher local oxygen concentration in the oxygenated MTBE blended fuel mixture will have an opposite effect and may confound the results.

Fuel density is seen in Table 4 to be lower for the MTBE blended fuel mixtures. The lower density will have an effect on fuel injection, effectively retarding and increasing the duration of the injection event. The retarded injection timing may be beneficial in reducing nitrogen oxide emissions, while the sustained injection may be beneficial in promoting soot oxidation through increased late combustion turbulence. The kinematic viscosity shown in Table 4 for the fuels are typical of liquids at 35 C. Liquid viscosity's decrease significantly as the temperature is raised. Table 4 shows the kinematic viscosity of the MTBE mixture to be lower than that of the corresponding pure diesel fuel. The lower viscosity MTBE-mixed fluid should help promote in-cylinder mixing through increased fuel breakup, which may have beneficial effects on soot oxidation and detrimental effects on nitrogen oxide emissions. Table 4 also shows a lower caloric value for the MTBE-mixed fuel. This lower heating value may be beneficial in promoting a lower formation rate of nitrogen oxide (which is temperature or energy dependant), resulting in lower exhaust nitrogen oxide emissions.

RESULTS AND DISCUSSION

STEADY-STATE OXYGEN ENRICHMENT DATA

Oxygen enrichment was conducted at both the 75% and 25% load conditions outlined in Tables 2 and 3.

75% load (Mode 6) oxygen enrichment results

Pressure traces for oxygen enrichment rates of 22% and 23% are shown in Fig. 6. As can be seen from the figure, at TVC=10, increased oxygen enrichment results in smaller ignition delays. Peak cylinder pressures are also higher. The results of heat release analysis are shown in Figs. 7 and 8.

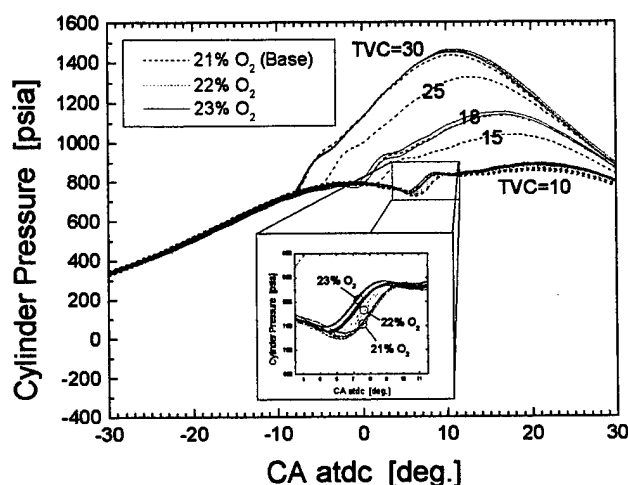


Figure 6. Steady-state pressure traces for mode 6 (75% load) baseline, 22% O₂, and 23% O₂ enrichment runs at TVC=10, 15, 18, 25, and 30.

The heat release rate traces in Fig. 7 also show smaller ignition delays with oxygen enrichment, as depicted by the earlier initial sharp rises in heat release rates with oxygen enrichment. As might be expected with the smaller ignition delay, the initial premix burn mode of combustion is also smaller with oxygen enrichment. NO_x tends to be proportionately related to the premix burn fraction. This proportional relationship is now speculated as an outcome of higher temperatures (normally associated with larger premix burn fractions) within the diffusion flame that surrounds the combusted premix burn fraction. Since smaller premixed burn combustion modes generally signify lower temperatures, the oxygen enrichment runs may be expected to have lower NO_x emissions. However, the enrichment may locally cause the normally rich premixed combustion event to be more stoichiometric, supporting higher formation rates of NO_x through higher local temperatures in the premix burn fraction and, hence, in the NO_x-forming diffusion flame. As with baseline mode-6 operation, Fig. 7 indicates that combustion with oxygen enrichment is also mixing controlled dominated. And, with oxygen enrichment, the rate of heat release is higher under the mixing controlled dominated combustion phase. The higher heat release rate may be due to a larger fraction of fuel being available for combustion. If the higher heat release rate in the mixing-

controlled burn mode leads to higher temperatures, the higher temperatures and increased local oxygen concentration within the mixing-controlled burn mode likely leads to lower particulate matter through an increase in oxidation of any formed soot.

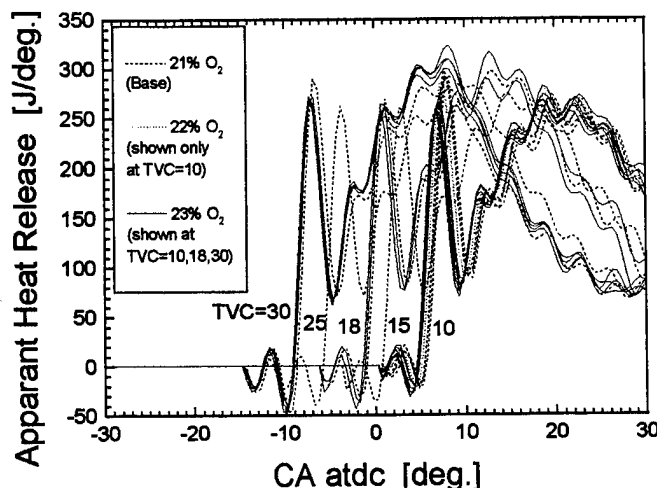


Figure 7. Steady-state gross apparent heat release rate traces for mode 6 (75% load) baseline, 22% O₂, and 23% O₂ enrichment runs at TVC=10, 15, 18, 25, and 30

Fig. 8 compares the normalized accumulative heat release traces under base and oxygen enriched runs. Again, the shorter ignition delay can be seen with oxygen enrichment. In comparing Figs. 7 and 8, the accumulative heat release is seen to be equivalent by the beginning of the mixing-controlled combustion phase. Therefore, entering into the mixing-controlled combustion phase, both base and oxygen enrichment runs have combusted the same amount of fuel. Note, though, that the combustion events are different. Figs. 7 and 8 show earlier heat releases yet slower heat release rates by the end of the premixed burn mode for the oxygen enrichment runs. However, the base runs end up releasing the same energy on entering into the mixing-controlled combustion phase since the premix and early diffusion burning is more brisk. Yet again, in the mixing-controlled phase of combustion up through 50% of the total heat release, the accumulative heat release is slightly larger with oxygen enrichment. The data seems to also indicate that, with oxygen enrichment, combustion ends earlier. However, after 50% of the accumulative heat release, runs at the TVC=18 timing are confounding and inconclusive. Possibly, after 50% of accumulative heat release, the physical, yet random, mixing process is the controlling mechanism for the combustion of fuel. However, although the rate of combustion may be similar by the end of the mixing-controlled combustion phase, the combustion environment (stoichiometry and temperature) may be quite different between base and oxygen enriched runs.

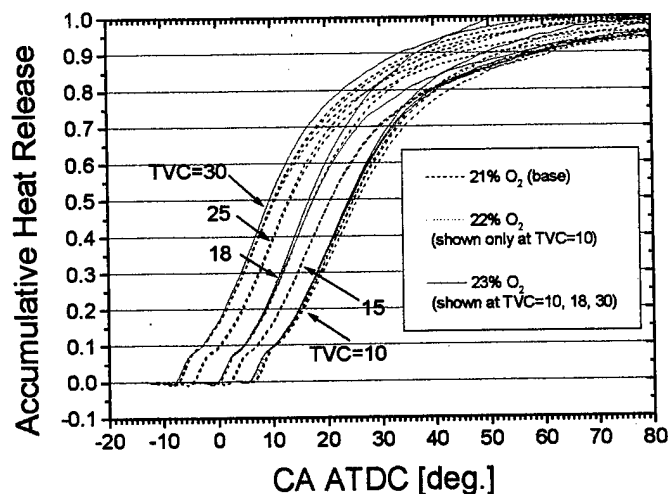


Figure 8. Steady-state, normalized accumulative heat release traces for mode 6 (75% load) baseline, 22% O₂, and 23% O₂ enrichment runs at TVC=10, 15, 18, 25, and 30.

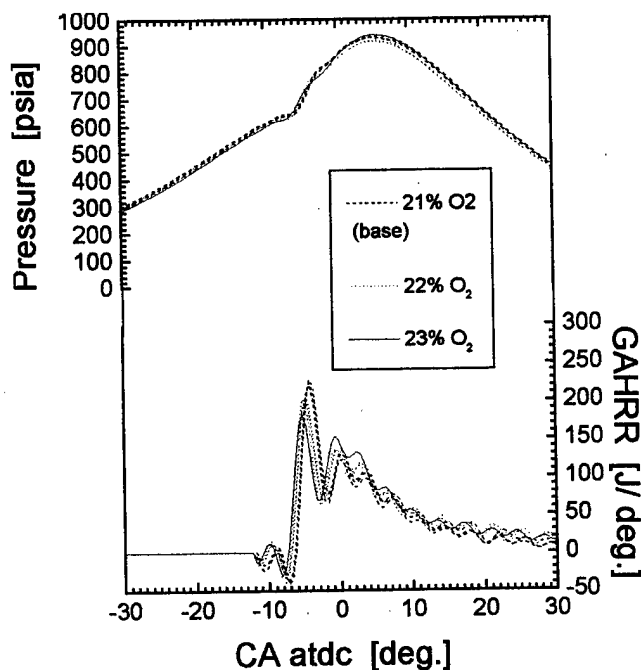


Figure 9. Steady-state cylinder pressure and gross apparent heat release rate (GAHRR) traces for a characterized low-load (25% load) operating condition [12] under baseline, 22% O₂, and 23% O₂ enrichment.

25% load oxygen enrichment results

25% load operation was run to study the effect oxygen enrichment has at different loads and to delineate trends with oxygen enrichment. Pressure traces for oxygen enrichment rates of 22% and 23% are shown in Fig. 9. As at the higher load, oxygen enrichment decreases the ignition delay and raises the peak cylinder pressure.

Unlike mode-6 operation, Fig. 9 indicates that both baseline and oxygen enrichment combustion at the low-load condition is premix burn combustion mode dominated. However, the heat release rate traces similarly show that the initial premix burn mode of combustion is smaller with oxygen enrichment, as might be expected with the smaller ignition delays. And, as at the higher load condition, the heat release rate in the mixing controlled combustion phase is higher with oxygen enrichment.

Since the premix burn dominates most of the total heat release at low load, it may have a larger impact on low load emissions. A smaller premixed burn combustion mode usually signifies lower temperatures. However, as at the higher load, the enrichment likely causes the normally rich premixed combustion event to be less rich, supporting higher formation rates of NO_x through higher local temperatures in the premix burn fraction and, hence, in the NO_x-forming diffusion flame. Normally, higher temperatures in the premixed burn phase will lead to higher soot through increased fuel pyrolysis. Nonetheless, fuel pyrolysis may also be diminished due to the increased oxidation brought about by the more stoichiometric combustion. If the higher heat release rate in the mixing-controlled burn mode leads to higher temperatures, the oxygen enriched combustion might also be expected to result in lower particulate matter through increased late cycle soot oxidation.

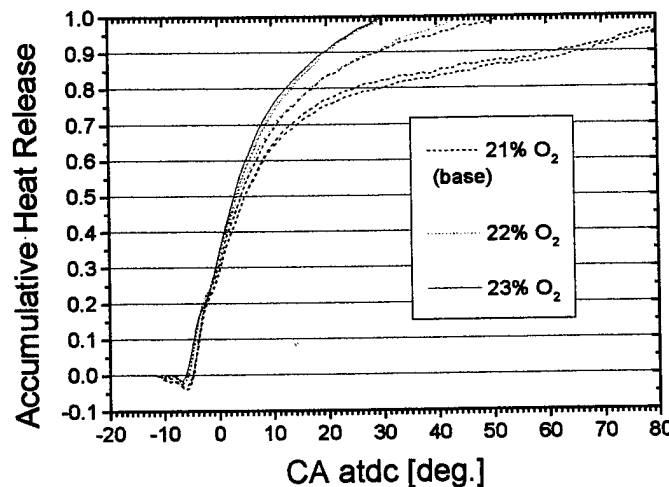


Figure 10. Steady-state, normalized accumulative heat release traces for a characterized low-load (25% load) condition [12] under baseline, 22% O₂, and 23% O₂ enrichment.

Fig. 10 compares the normalized accumulative heat release traces under base and oxygen enriched runs at the low load condition. Again, the shorter ignition delay can be seen with oxygen enrichment. In comparing the heat release results shown in Figs. 9 and 10, the accumulative heat release is again seen to be equivalent by the beginning of the mixing-controlled combustion phase, as was noted for high load operation. Therefore, entering into the mixing-controlled combustion phase, both base and oxygen enrichment runs have combusted the same amount of fuel. Note, though, that the combustion events are different. Figs. 9 and 10 show earlier heat releases yet slower heat release rates by the end of the premixed

burn mode for the oxygen enrichment runs. However, the base runs end up releasing the same energy on entering into the mixing-controlled combustion phase since the premix and early diffusion burning is more brisk. Yet again, in the mixing-controlled phase of combustion, the accumulative heat release is larger with oxygen enrichment. The data also clearly indicate that combustion ends earlier with oxygen enrichment.

STEADY-STATE OXYGENATED FUEL DATA

Pressure traces for base and MTBE oxygenated fuels are shown in Fig. 11 for mode-6 operation at TVC=10, 18, and 30. The oxygenated fuel can be seen to retard the start of combustion. However, the retarded start of combustion is misleading since its delay is due primarily to a retarded start of injection caused by the lower density of the oxygenated fuel mixture. Except for the most retarded timing, at TVC=10, the ignition delay is similar between the base and oxygenated fuel mixture. At TVC=10, the ignition delay is longer for the oxygenated fuel. Fig. 11 also indicates that the oxygenated fuel results in a lower peak cylinder pressure. The lower peak cylinder pressure is likely due to the lower heating value of the oxygenated fuel mixture.

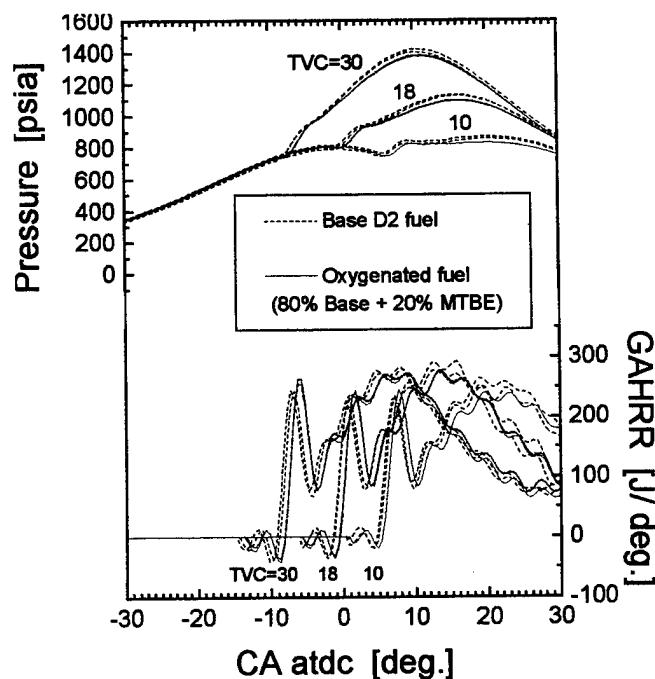


Figure 11. Steady-state cylinder pressure and gross apparent heat release rate (GAHRR) traces for mode 6 (75% load) operation at TVC=10, 18, and 30 using baseline D2 fuel and oxygenated fuel (80% base D2 + 20% MTBE).

The heat release rate traces in Fig. 11 also show that the initial premix burn mode of combustion is larger with the oxygenated fuel mixture, as might be expected since the MTBE blended fuel has a larger fraction of lower boiling point temperature components (shown in Fig. 5). The larger premixed burn combustion

modes generally signify higher temperatures. Additionally, as with oxygen enrichment, the oxygenated fuel may locally supply more oxygen to the hydrocarbon fuel radicals causing the normally rich premixed combustion event to be less rich, supporting higher formation rates of NO_x through higher local temperatures in the premix burn fraction and, hence, in the NO_x-forming diffusion flame.. However, although the heat release in the premixed burn was greater than that under base operation, the lower heating value of the oxygenated fuel mixture may actually diminish in-cylinder temperatures.

As Fig. 11 shows, the rate of heat release for the oxygenated fuel is lower in the mixing controlled combustion phase compared with that for the base fuel, possibly due in part to more fuel having been burned in the premixed combustion mode. The lower heat release rate is also due, in part, to the lower heating value of the oxygenated fuel. Although speculative, the increased local oxygen concentration within the mixing-controlled burn mode with oxygen enrichment may beneficially help lead to lower soot through an increase in oxidation of any formed soot. Therefore, both the premix and mixing-controlled burn modes appear to support the lower particulate matter emissions.

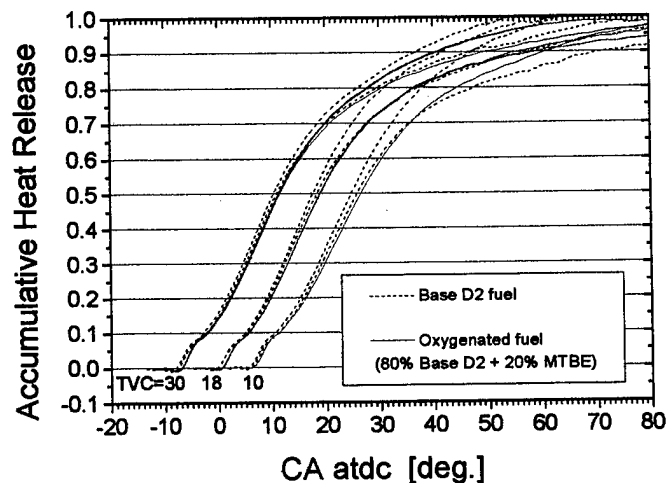


Figure 12. Steady-state, normalized accumulative heat release traces for mode 6 (75% load) operation at TVC=10, 18, and 30 using baseline D2 fuel and oxygenated fuel (80% base D2 + 20% MTBE).

Fig. 12 compares the normalized accumulative heat release traces under base and oxygenated fuel runs at the mode-6 conditions. Again, longer ignition delays can be seen with the oxygenated fuel mixtures. However, the combustion events appear similar. The only difference being in phasing due to the different start-of-combustion's. Similar heat release is seen up through 50% of the total heat release. The data is inconclusive beyond 50% of the total heat release. The physical yet random mixing process of the mixing-controlled dominated combustion event seems to be the controlling mechanism for the late cycle combustion of the two tested fuels. The nature of heat release beyond 50% of the total heat release is likely due to different rates of mixing.

EMISSION COMPARISON

Fig. 13 graphically summarizes the effects of base and oxygenated fuels, as well as that of oxygen enrichment, on NO_x and particulate matter emissions at the 75% high load mode-6 operating condition. A summary of 17 sweeps is depicted by the parabolic curves shown in the figure. The solid diamonds represent base timing runs that were taken prior to the oxygenated fuel-timing sweeps. Each "x" and "+" represents the emissions under oxygenated fuel operation. Twenty two percent and 23% oxygen enrichment runs are denoted with the open triangle and square symbols, respectively. Electronic TVC fuel injection timing is noted next to the data points.

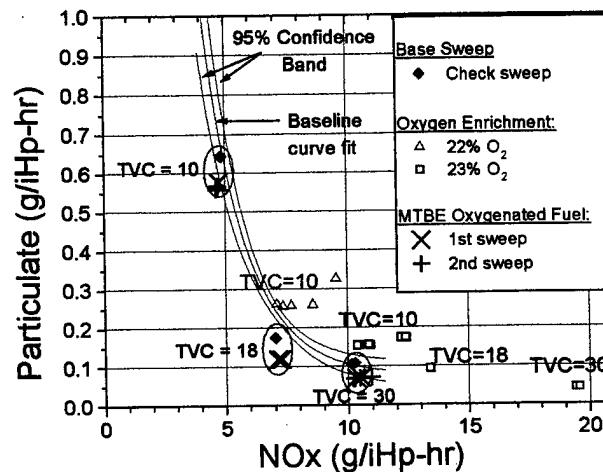


Figure 13. Comparison of NO_x-particulate trade-off curves for baseline, oxygen enrichment (22% and 23% O₂) and 20% MTBE Oxygenated Fuel Run cases at mode-6 75% load.

Comparison of base and oxygenated fuel runs may be made at specific fuel injection timings as depicted by the encircled data points in Fig. 13. Fig. 13 indicates that particulate matter emissions are reduced with the oxygenated fuel. However, the oxygenated fuel has little effect on NO_x emissions.

As can be seen from the 75% high load data shown in Fig. 13, measured NO_x concentrations varied over a wide range of values with oxygen enrichment. This was due to the feedback control system used to control the oxygen enrichment. The sampling of the intake surge tank took time. When the measured oxygen concentration fell outside acceptable limits, adjustments were made to the oxygen flow rate. Again, sampling was performed and new adjustments made. Due to the high sensitivity of NO_x formation to oxygen concentration, and the lack of precise closed-loop oxygen enrichment control, the measured NO_x emissions varied with time over the allotted time required to obtain particulate matter data. The figure demonstrates that oxygen enrichment dramatically increases NO_x emissions. Also, for retarded timings such as TVC=10, particulate matter emissions are initially drastically reduced. Increasing the concentration of oxygen from 21% to 22% at a TVC=10 timing is seen to drop particulate matter to levels below that seen at a TVC=15 timing. However, after 23% oxygen enrichment, the benefits of oxygen enrichment to

particulate matter emissions are slight, while the unfavorable effects on NOx emissions are great. The benefits of oxygen enrichment at advanced timings are less. At a TVC=30 advanced timing and a 23% oxygen enrichment, particulate matter is reduced by less than 0.1 g/ihp-hr. However, NOx emissions are seen to increase by about 5 g/ihp-hr.

The effects of oxygen enrichment on emissions at the 25% low load condition are outlined in Table 5. As at the higher load condition (mode-6), oxygen enrichment is seen to increase NOx emissions and decrease particulate matter. The effects of oxygen enrichment on CO and CO₂ emissions are small, but inconclusive.

TABLE 5: LOW-LOAD EMISSIONS UNDER OXYGEN ENRICHMENT

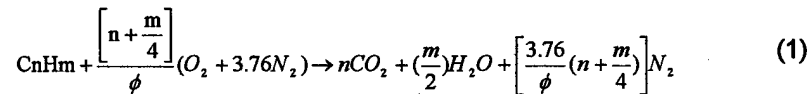
Emission	Units	21% O ₂	23% O ₂	25% O ₂
NO _x	(g/iHp-hr)	16.99	29.60	30.53
	(g/bhp-hr)	22.91	39.60	41.53
Particulate	(g/iHp-hr)	0.0886	0.0619	0.0504
	(g/bhp-hr)	0.1193	0.0828	0.0686
CO	(ppm)	68.93	63.52	64.03
CO ₂	(%)	3.61	3.55	3.65

ANALYSIS OF BASE, OXYGENATED FUEL, AND OXYGEN ENRICHMENT COMBUSTION

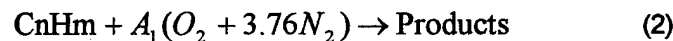
As can be seen from Fig. 13, the effects of the oxygenated fuel on both NOx and particulate matter emissions are less than that observed under oxygen enrichment. To explain the observed differences, an elementary analysis, using a number of assumptions, is conducted on the different oxygen enhancing methods to decipher the differences in the local fuel plume environment and in the overall in-cylinder gas composition.

BASE DIESEL FUEL COMBUSTION

A generic fuel molecule, C_nH_m, with n carbon and m hydrogen atoms, reacts completely according to the following equation, Eq. (1), where ϕ is either the overall or local equivalence ratio, depending on whether the equation represents an overall or local reaction:

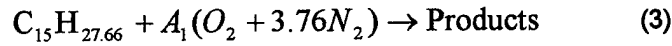


In the above equation, 4.76 moles of air is assumed to be composed only of one mole of oxygen (O₂) and 3.76 moles of nitrogen (N₂). The above equation may be simplified as:



$$\text{where } A_1 = \frac{\left[n + \frac{m}{4} \right]}{\phi}$$

Assuming a mole of the diesel fuel has on average 15 carbon atoms and 27.66 hydrogen atoms, the reaction for one mole of fuel would be:



$$\text{with } A_1 = \frac{21.915}{\phi}$$

In the fuel plume, combustion is believed to be rich ($\phi > 1$). If all fuel is assumed vapor and to obey the ideal gas law, the volume of the fuel plume (V_{plume}) is composed of a volume of fuel (V_{fuel}) and a local reacting volume of air (V_{air}) which may be related as follows:

$$V_{\text{plume}} - V_{\text{fuel}} = V_{\text{air}} \quad (4)$$

The moles of reacting air may be equated to these volumes as follows:

$$4.76 * A_1 = \frac{V_{\text{plume}}}{V_{\text{fuel}}} - 1 = \frac{V_{\text{plume}}}{\frac{M_{\text{fuel}}}{\rho_{\text{vapor},1}}} - 1 = \frac{V_{\text{air}}}{V_{\text{fuel}}} \quad (5)$$

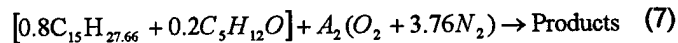
The local carbon to oxygen ratio for base diesel fuel combustion, $C/O|_{\text{Base}}$, can be obtained from Eq. (3) and is the following:

$$C/O|_{\text{Base}} = \frac{15}{2 * A_1} \quad (6)$$

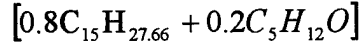
Comparing the carbon-oxygen ratios (for base, oxygenated fuel, and oxygen enrichment cases) will indicate which case has locally more oxygen in the fuel plume.

OXYGENATED FUEL (20% MTBE) COMBUSTION

With the 20% MTBE ($C_5H_{12}O$) oxygenated fuel, referred to as fuel-2, a reaction equation similar to Eq. (3) may be written as follows:



where one mole of fuel-2 is:



Also, an equation similar to Eq. (5) may be written, where the mass flow rate of fuel-2 is equal to that under base fuel operation:

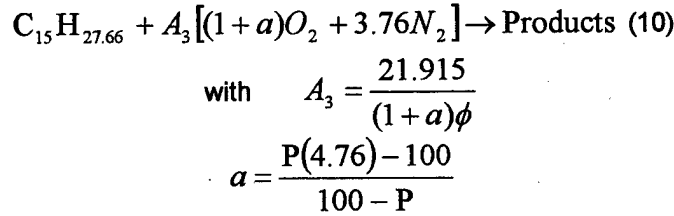
$$4.76 * A_2 = \frac{V_{plume}}{V_{fuel,2}} - 1 = \frac{V_{plume}}{\frac{M_{fuel}}{\rho_{vapor,2}}} - 1 = \frac{V_{air}}{V_{fuel,2}} \quad (8)$$

With the oxygenated fuel, fuel-2, the local carbon to oxygen ratio, $C/O|_{MTBE}$, is the following:

$$C/O|_{MTBE} = \frac{(0.8)(15) + (0.2)(5)}{2 * A_2 + 0.2} = \frac{13}{2 * A_2 + 0.2} \quad (9)$$

23% OXYGEN ENRICHMENT COMBUSTION

With oxygen enrichment, the local reaction equation may be written as follows:



and $P = \text{percent oxygen enrichment (\%)}$

In this analysis, only the 23% oxygen enrichment case is considered. Therefore, $P=23$ and $a=0.1231$.

Again, an equation similar to Eq. (5) may be written, this time for oxygen enrichment:

$$A_3(4.76 + a) = \frac{V_{plume}}{V_{fuel}} - 1 = \frac{V_{plume}}{\frac{M_{fuel}}{\rho_{vapor,1}}} - 1 = \frac{V_{air}}{V_{fuel}} \quad (11)$$

With oxygen enrichment, the local carbon to oxygen ratio, $C/O|_{23\%O_2}$, is the following:

$$C/O|_{23\%O_2} = \frac{15}{2 * A_3(1.123)} = \frac{13.3557}{2 * A_3} \quad (12)$$

COMPARISON OF BASE, OXYGENATED FUEL, AND OXYGEN ENRICHMENT CASES

Comparing the carbon-oxygen ratios (for base, oxygenated fuel, and oxygen enrichment cases) will indicate which condition has locally more oxygen in the fuel plume. Pyrolysis, hence soot, is less likely with higher local oxygen concentrations. Therefore, since soot emissions decrease from base to oxygenated fuel to oxygen enriched combustion, the local oxygen concentration inside the plume is assumed to increase from base to oxygenated fuel to oxygen enriched combustion. The analysis below estimates the local oxygen concentration for the base, oxygenated fuel, and oxygen enriched combustion cases and examines the relative effectiveness of the oxygen enhanced combustion methods.

Recognizing that the local combustion is likely rich, $\phi \sim 2$ to 4 [17], or at least stoichiometric, $\phi = 1$, then Eq. (3) indicates that $5.479 \leq A_1 \leq 21.915$. Therefore, Eq. (6) dictates that:

$$\begin{aligned} 0.342 \leq \left. \frac{C}{O} \right|_{Base} &\leq 1.369 \\ \text{or} \\ 0.730 \leq \left. \frac{O}{C} \right|_{Base} &\leq 2.922 \end{aligned}$$

Comparison of base and oxygenated fuel cases

Dividing Eq. (6) by Eq. (9), the following equation is obtained:

$$\frac{\left. \frac{C}{O} \right|_{Base}}{\left. \frac{C}{O} \right|_{MTBE}} = \frac{\left[\frac{15}{2 * A_1} \right]}{\left[\frac{13}{2A_2 + 0.2} \right]} = \frac{30A_2 + 3}{26A_1} = \left(\frac{15}{13} \right) \left(\frac{A_2}{A_1} \right) + \left(\frac{3}{26A_1} \right) \quad (13)$$

To estimate the magnitude of A_2/A_1 , Eq. (5) may be divided by Eq. (8). The following equation is obtained since the mass rate of fuel was held constant and the plume volumes, V_{plume} , are assumed similar:

$$\frac{4.76A_1 + 1}{4.76A_2 + 1} = \frac{\rho_{vapor,1}}{\rho_{vapor,2}} \quad (14)$$

Assuming similar local pressure and temperatures, the fuel density is proportional to its molecular mass (MM). Therefore,

$$\frac{4.76A_1 + 1}{4.76A_2 + 1} = \frac{\rho_{vapor,1}}{\rho_{vapor,2}} = \frac{MM_1}{MM_2} = \frac{207.66}{183.73} = 1.13 \quad (15)$$

Eq. (13) and Eq. (15) may be combined, as follows:

$$\frac{C/O|_{Base}}{C/O|_{MTBE}} = 1.0209 + \frac{1}{1.1437(A_1)} \quad (16)$$

Since the above analysis has already shown that $5.479 \leq A_1 \leq 21.915$, then

$$6.1 < \frac{C/O|_{Base}}{C/O|_{MTBE}} < 18.0 \quad (17)$$

That is, the 20% MTBE oxygenated fuel is assessed to have between a 6.1% to 18% higher local oxygen concentration in the fuel plume than regular diesel. Eq. (15) estimates the range of A_2 to be between 4.823 and 19.365. Therefore, Eq. (9) dictates the following:

$$\begin{aligned} 0.334 &\leq C/O|_{MTBE} \leq 1.320 \\ &\text{or} \\ 0.757 &\leq O/C|_{MTBE} \leq 2.995 \end{aligned}$$

Comparison of base and oxygen enrichment cases

Dividing Eq. (6) by Eq. (12) results in the following equation:

$$\frac{C/O|_{Base}}{C/O|_{23\%O_2}} = \left(\frac{15}{13.356} \right) \frac{A_3}{A_1} \quad (18)$$

The ratio of A_3/A_1 can be obtained by dividing Eq. (5) by Eq. (11). Mass of fuel cancels since the mass flow rate of fuel was held constant between base and oxygen enrichment cases. Also, since the same base fuel is used in both case studies, fuel density is identical. The plume volumes are assumed equal. Under the above assumptions, the resulting equation is as follows:

$$\frac{4.76A_1 + 1}{A_3(4.76 * a) + 1} = 1 \quad (19)$$

Rearranging, recognizing $a=0.1231$ for 23% oxygen enrichment, the magnitude of A_3/A_1 is 0.97479. Therefore, Eq. (18) becomes

$$\frac{C/O|_{Base}}{C/O|_{23\%O_2}} = \left(\frac{15}{13.356} \right) (0.97479) = 1.0948 \quad (20)$$

Therefore, 23% oxygen enrichment adds locally approximately 9.5% more oxygen in the fuel plume versus baseline operation. Since $5.479 \leq A_1 \leq 21.915$, then $5.341 \leq A_3 \leq 21.362$. Therefore, Eq. (12) dictates the following:

$$\begin{aligned} 0.312 &\leq C/O|_{23\%O_2} \leq 1.250 \\ \text{or} \\ 0.799 &\leq O/C|_{23\%O_2} \leq 3.199 \end{aligned}$$

Comparison of 20% MTBE oxygenated fuel and 23% oxygen enrichment

The ratio of the carbon-oxygen ratios for 20% MTBE oxygenate fuel and 23% oxygen enrichment can be obtained by dividing Eq. (12) by Eq. (9), as follows:

$$\frac{C/O|_{23\%O_2}}{C/O|_{MTBE}} = \left(\frac{13.356}{13} \right) \left[\frac{2A_2 + 0.2}{2A_3} \right] = 1.02736 \left(\frac{A_2}{A_3} + \frac{1}{10A_3} \right) \quad (21)$$

The ratio of A_2/A_3 can be obtained by dividing Eq. (8) by Eq. (11). Mass of fuel cancels since the mass flow rate of fuel was held constant between 23% oxygen enrichment and 20% MTBE oxygenate fuel cases. Plume volumes are again also assumed similar and cancel. The oxygenated fuel does, though, have a lower density. However, assuming the ideal gas law holds, the fuel vapor density is proportional to molecular mass. Therefore, the resulting equation is the following:

$$\frac{4.76A_2 + 1}{A_3(4.76 * a) + 1} = \frac{\rho_{vapor,2}}{\rho_{vapor,1}} = \frac{MM_2}{MM_1} = \frac{183.73}{207.66} = 0.88475 \quad (22)$$

Substituting Eq. (22) into Eq. (21) results in the following:

$$\frac{C/O|_{23\%O_2}}{C/O|_{MTBE}} = 0.9325 + \left(\frac{1}{12.843A_3} \right) \quad (23)$$

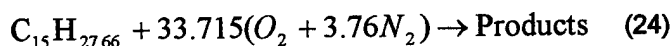
As stated earlier, A_3 should be between 5.341 and 21.362. Therefore, Eq. (23) indicates that the 20% MTBE oxygenated fuel operation has between 93.6% to 94.7% of the local oxygen concentration seen by the 23% oxygen enrichment operation. Or, inversely, 23% oxygen enrichment operation has approximately between a 5.6% to 6.8% higher local oxygen concentration within the fuel plumes than does 20% MTBE

oxygenated fuel operation. Since the range is small, the 23% oxygen enrichment operation is assumed to have on average a 6.2% higher oxygen concentration than that seen by 20% MTBE oxygenated fuel operation.

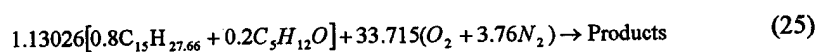
Base, oxygenated fuel, and oxygen enrichment case summary

As mentioned earlier, the 20% MTBE oxygenated fuel was projected to have between 6.1% to 18% higher local oxygen concentration in the fuel plume than that with base operation. Since 23% oxygen enrichment has approximately 9.5% more local oxygen than base operation and 6.2% more local oxygen than 20% MTBE oxygenated fuel operation, then the above ratios indicate that the 20% MTBE oxygenated fuel operating mode should have approximately 3.1% more oxygen than base operation. The 3.1% estimate falls outside the 6.1 to 18% range estimated in the original analysis for the 20% MTBE oxygenated fuel. This discrepancy in estimates is likely due to the simplification assumptions applied to this elementary analysis. The 20% MTBE oxygenated fuel likely has approximately between a 3.1 and 6.1% higher local oxygen concentration in the fuel plume than that under base operation. Therefore, this analysis indicates that the 23% oxygen enrichment operation supplies nearly double the local oxygen in the spray plume than does the 20% MTBE oxygenated fuel operation.

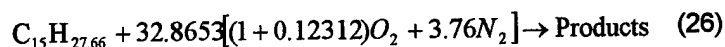
An analysis can also be conducted on the overall content within the cylinder. The base mode-6 operating condition has an approximate overall equivalence ratio of 0.65. In running the 20% MTBE oxygenated fuel and 23% oxygen enrichment cases, mass fueling rate and intake pressure were held equal to that under base operation. Using Eq. (3), the overall base reaction equation is the following:



Assuming a similar mass flow rate, an equation similar to Eq. (7) may be written for the overall reaction of the lower density 20% MTBE oxygenated fuel:



Under 23% oxygen enrichment, an equation similar to Eq. (10) may be used for the overall reaction equation. However, since oxygen was added to boost the intake to 23% oxygen, while fuel flow rate and intake pressure were maintained at base operating conditions, A_3 can not be calculated with an overall equivalence ratio of 0.65. Under equivalent intake pressure and assumed temperatures, the moles of air under base operation must equal the moles of "air" under oxygen enriched conditions. Therefore, the overall reaction equation under 23% oxygen enriched combustion becomes:



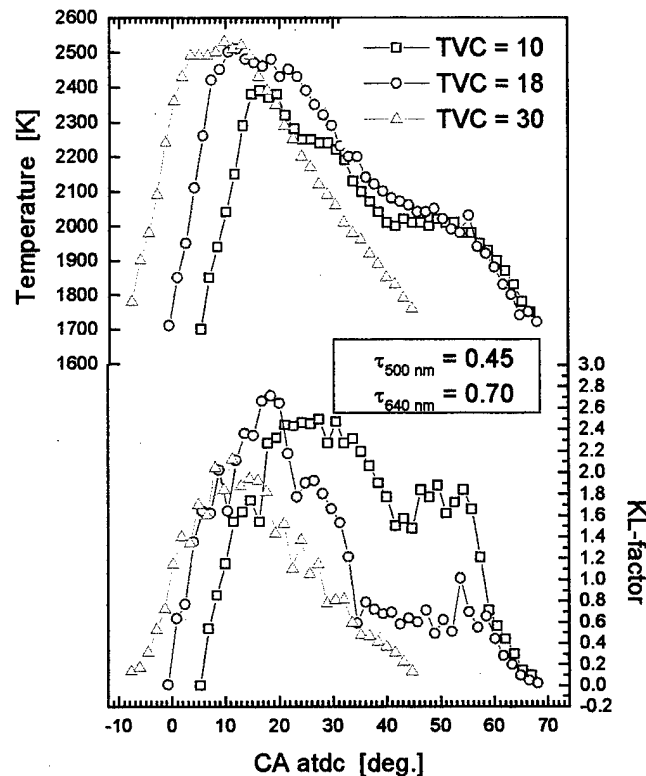


Figure 14. Variation in two-color output (view-averaged temperatures and KL-factors) for mode 6 (75% load) operation at three different TVC injection timings (3rd combustion event).

Therefore, overall, the 20% MTBE oxygenated fuel has a 0.3% higher oxygen concentration than that under base operation. But, locally, the 20% MTBE oxygenated fuel has approximately a 4.6% (actually estimated between 3.1 and 6.1%) higher oxygen concentration than that under base operation. Similarly, 23% oxygen enrichment has overall and locally a 9.5% higher oxygen concentration than that under base operation. Between 20% MTBE oxygenated fuel and 23% oxygen enriched combustion, the 23% oxygen enriched combustion has overall a 9.1% higher oxygen concentration. However, locally, the 23% oxygen enriched combustion has a 6.2% higher oxygen concentration than that under 20% MTBE oxygenated fuel operation.

TWO-COLOR DATA

The two-color method is a measuring technique used to obtain the soot temperature and concentration inside a flame. Since the diesel engine produces soot, where the temperature of the soot offers a good description of the in-cylinder temperatures, the two-color technique is applicable in obtaining in-cylinder flame temperatures and soot concentrations. A detailed derivation of the two-color method can be found in

the Appendix. This section will present the two-color data for baseline, 20% MTBE oxygenated fuel, and 23% oxygen enriched combustion.

Filmed mode-6 baseline data

The baseline data in Fig. 14 presents view-averaged data for the third combustion event. The temperature and KL-factor data shown at each TVC injector timing are similar, although shifted in phasing. With timing retard, in-cylinder temperatures remain higher later into the combustion cycle. The average KL-factors for each specific temperature range are also generally larger later into the combustion cycle with timing retard.

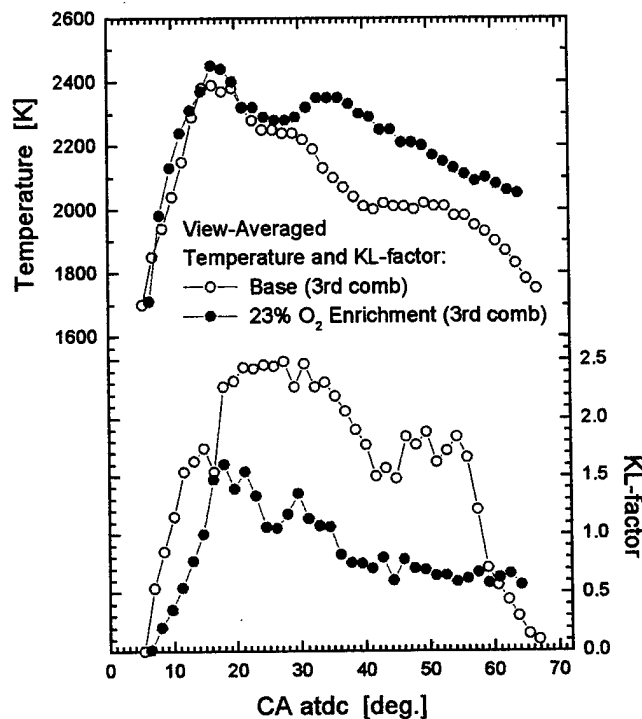


Figure 15. Variation in two-color output between mode-6 baseline (75% load, 21% O₂) operation (3rd combustion) and mode-6 oxygen enrichment (75% load, 23% O₂) operation (3rd combustion) at TVC=10 injection timing ($\tau_1=0.45$, $\tau_2=0.70$).

Filmed oxygen enrichment data

As shown in Fig. 15, for TVC=10, the two-color baseline data presented in Fig. 14 are compared with filmed 23% oxygen enrichment data. Fig. 15 suggests that the in-cylinder temperatures are higher and KL-factors are lower, especially noticeable within the mixing-controlled dominated portion of the combustion cycle (between 20 and 60 CA° atdc).

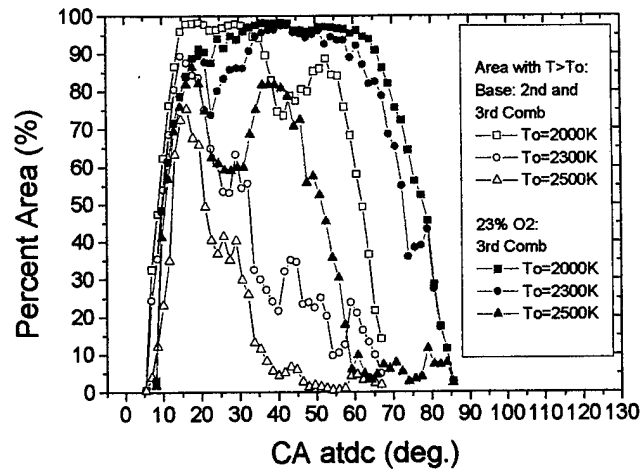


Figure 16. Two-color base (21% O₂, 3rd combustion) and oxygen enrichment (23% O₂, 3rd combustion) temperature data for mode-6 (75% load) at TVC=10 ($\tau_1=0.30$, $\tau_2=0.78$).

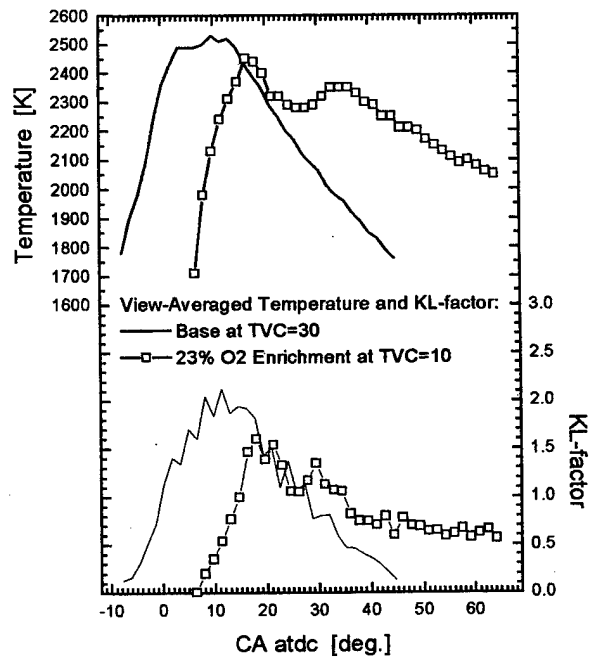


Figure 17. Comparison between mode-6 baseline (75% load, 21% O₂) operation (3rd combustion) at TVC=30 and mode-6 oxygen enrichment (75% load, 23% O₂) operation (3rd combustion) at TVC=10 injection timing ($\tau_1=0.45$, $\tau_2=0.70$).

Further differences with oxygen enrichment can be observed by Fig. 16, which shows the percent of the viewed area covered by the different temperature regimes. After the initial combustion, a much larger field of view is covered by the different temperature regimes under oxygen enrichment. The higher exhaust NO_x emissions with oxygen enrichment are understandable since a much larger fraction of the bulk gas partakes in the high temperature combustion process, as inferred from the larger field of view covered by soot emissions.

The data in Fig. 13 showed that TVC=30 baseline operation has similar NO_x emissions to TVC=10 23% oxygen enrichment operation. However, even though particulate emissions are drastically reduced from the TVC=10 baseline timing condition, the TVC=10 23% oxygen enriched particulate matter emissions is slightly higher than that under TVC=30 baseline operation. Fig. 17 compares the view-averaged two-color output for the TVC=30 baseline and TVC=10 23% oxygen enriched operating conditions. The figure shows similar histories in temperature and KL-factors, although shifted in phasing. The similar time and magnitude of high temperature combustion likely explains, in part, the similar NO_x emissions. However, the data only indicate the thermal effect of oxygen enrichment. A dilution-effect probably also plays a role. The higher late-cycle KL-factors are consistent with the observed slightly higher exhaust particulate emissions.

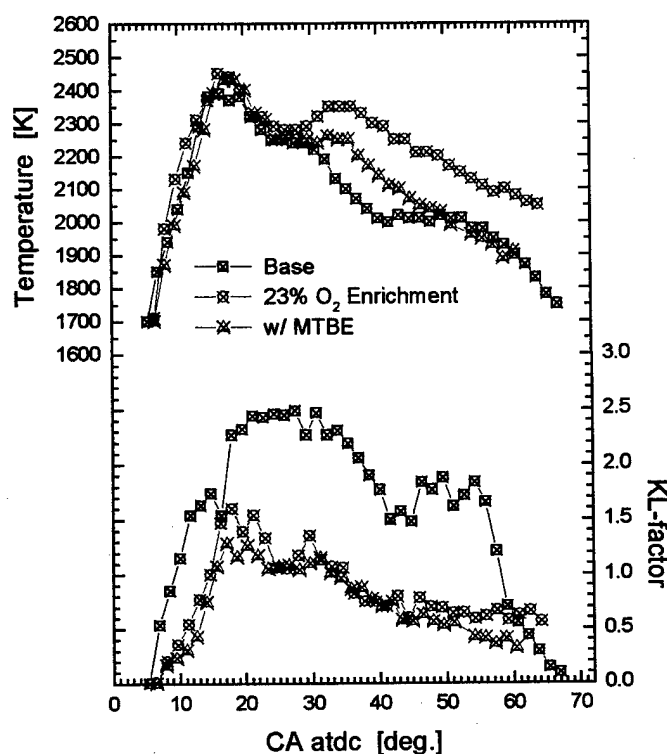


Figure 18. View-averaged two-color temperature and KL-factor comparisons of base, oxygen enrichment, and oxygenated fuel (w/ MTBE) runs under mode-6 operation at TVC=10. Optic spectral transmissivities at 0.45 and 0.70.

Filmed oxygenated fuel data

Fig. 18 compares, for TVC=10, the view-average two-color baseline, 23% oxygen enrichment, and 20% MTBE oxygenated fuel operation data. Fig. 18 suggests that, during the mixing-controlled portion of combustion, the in-cylinder temperatures are highest with 23% oxygen enrichment and lowest with baseline operation. The 20% MTBE oxygenated-fuel operating temperatures are similar, but higher, than baseline operation. Inversely, the highest KL-factors are seen with baseline operation. Differences in KL-

factor between 23% oxygen enrichment and 20% MTBE oxygenated fuel operation are hard to distinguish, although KL-factors generally appear slightly higher for 23% oxygen enrichment.

Fig. 19 shows the maximum in-cylinder two-color temperatures obtained under baseline, 20% MTBE oxygenated fuel, and 23% oxygen enrichment operation. As with the average two-color data, the maximum temperatures are seen with 23% oxygen enrichment, followed by 20% MTBE oxygenated fuel operation, with the lowest temperatures seen under baseline operation.

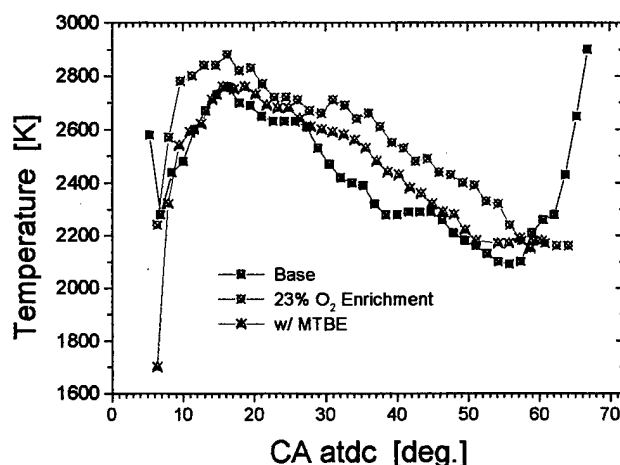


Figure 19. Maximum two-color temperature and KL-factors for base, oxygen enrichment, and oxygenated fuel (w/ MTBE) runs under mode-6 operation at TVC=10. Optic spectral transmissivities at 0.45 and 0.70.

SUMMARY

Increasing the concentration of oxygen from 21 to 22% by oxygen enrichment drastically reduces particulate matter emissions while only moderately increasing NOx emissions, the exact magnitudes depending on injection timing. However, after 23% oxygen enrichment, the increased benefits of oxygen enrichment to particulate matter emissions are slight, while the unfavorable effects on NOx emissions are great. At both loads, oxygen enrichment decreased ignition delay and raised the peak cylinder pressure, but was found to have no large effect on performance. Unlike oxygen enrichment, the oxygenated fuel was found to reduce particulate matter emissions and have little effect on NOx emissions. Under 75% load retarded timing operation, known to be high sooting, a 20% MTBE mixture was only found to reduce particulate by 14%. Further improvements would be gained by running neat MTBE.

An elemental analysis of the base, 20% MTBE oxygenated fuel, and 23% oxygen enrichment operating conditions demonstrated that the oxygenated fuel and oxygen enriched operations add locally approximately 4.6 and 9.5% more oxygen, respectively, than that under base operation. Hence, the experimental data give validity to the conclusion that higher local oxygen concentrations reduce fuel pyrolysis and increase soot oxidation. The elemental analysis also found, globally, that the oxygenated fuel

has little effect on the bulk cylinder gas oxygen concentration. However, oxygen enrichment has a large dilution effect, having overall (and locally) a 9.5% higher oxygen concentration than that under base operation, favorably promoting NO_x formation since as much as half of all NO_x is formed in the bulk post-combustion cylinder gas.

Two-color analysis of oxygen enrichment confirms that a much larger fraction of the bulk gas does partake in high temperature combustion, likely due to an increase in oxygen. Two-color data showed that the in-cylinder temperatures are highest with 23% oxygen enrichment, followed by the 20% MTBE oxygenated fuel, and then base fuel operation. Inversely, KL-factors (or soot) are highest with baseline operation. Differences in KL-factors between the oxygen enhancing methods are inconclusive.

CONCLUSION

Oxygen enrichment has a similar effect with load on engine output. Oxygen enrichment detrimentally increases NO_x through increased temperatures and oxygen concentration and decreases particulate through reduced fuel pyrolysis and increased soot oxidation. The magnitudes of these effects differ, however, due to the differences in fuel loading.

The MTBE oxygenated fuel mixture has a lower density and a higher fraction of higher volatile components compared to the base diesel fuel. The ignition delays are similar for both base fuel and oxygenated fuel mixture. The observed retarded start of combustion with the MTBE mixture is misleading since its delay is due primarily to a retarded start of injection caused by the lower density of the oxygenated fuel mixture. Likewise, the lower peak cylinder pressure with the oxygenated fuel is likely due to the lower heating value of the oxygenated fuel mixture. The initial premix burn mode of combustion is larger with the oxygenated fuel mixture since the MTBE blended fuel has a larger fraction of lower boiling point temperature components.

The analysis indicates that the improvement in the exhaust emissions depended almost entirely on the local oxygen concentration in the fuel plume, regardless of the method of oxygen enhancement. Oxygen enrichment had a larger reducing effect on the particulate matter emissions due to the locally larger concentration of oxygen in the fuel plume. The oxygenated fuel would likely have achieved a similar reduction with comparable oxygen loading. As discussed in the literature review, research with oxygenated fuel agents has similarly shown emissions and performance to be almost entirely dependant on the oxygen content in the fuels, regardless of the oxygenate to diesel fuel blend ratios and the type of oxygenate.

REFERENCES

1. Miyamoto, N., Ogawa, H., Nurun, N., Obata, K., and Arima, T., "Smokeless, Low NO_x, High Thermal Efficiency, and Low Noise Diesel Combustion with Oxygenated Agents as Main Fuel," SAE Paper 980506, 1998.
2. Maricq, M., Chase, R., Podsiadlik, D., Siegl, W., and Kaiser, E., "The Effect of Dimethoxy Methane Additive on Diesel Vehicle Particulate Emissions," SAE Paper 982572, 1998.
3. Liotta, F., and Montalvo, D., "The Effect of Oxygenated Fuels on Emissions from a Modern Heavy-Duty Diesel Engine," SAE Paper 932734, 1993.
4. Choi, C., Bower, G., and Reitz, R., "Effects of Biodiesel Blended Fuels and Multiple Injections on D.I. Diesel Engine Emissions," SAE Paper 970218, 1997.
5. Ali, Y., and Hanna, M., "In-Cylinder Pressure Characteristics of a D.I. Heavy Duty Diesel Engine on Biodiesel Fuel," SAE Paper 971683, 1997.
6. Chang, D., and Van Gerpen, J., "Fuel Properties and Engine Performance for Biodiesel Prepared from Modified Feedstocks," SAE Paper 971684, 1997.
7. Kajitani, S., Chen, Z., Konno, M., and Rhee, K., "Engine Performance and Exhaust Characteristics of Direct-Injection Diesel Engine Operated with DME," SAE Paper 972973, 1997.
8. Li, J., Chae, J., Park, S., Paik, H., Park, J., Jeong, Y., Lee, S., and Choi, Y., "Effect of Intake Composition on Combustion and Emission Characteristics of DI Diesel Engine at High Intake Pressure," SAE Paper 970322, 1997.
9. Watson, H., Milkins, E., and Rigby, G., "A New Look at Oxygen Enrichment 1) The Diesel Engine," SAE Paper 900344, 1990.
10. Ghajel, J., Hilliard, J., and Levendis, J., "The Effect of Oxygen Enrichment on the Performance and Emissions of I.D.I. Diesel Engines," SAE Paper 830245, 1983.
11. Chicago Tribune, sect. 2, pg. 1, "Argonne Idea May Make Diesels Less Dirty," by Jon Van, September 26, 1998.
12. Dec, J., "A Conceptual Model of DI Diesel Combustion Base on Laser-Sheet Imaging," SAE Paper 970873, 1997.
13. Muller, K., "Influence of Engine Design and Fuel Quality on Diesel Emissions. II: Fuel Quality," Ninth World Petroleum Congress Proceedings, 6, 199, 1975.
14. Broering, L.C., and Holtman, L. W., "Effect of Diesel Fuel Properties on Emissions and Performance," SAE Paper 740692 1974.

15. Barry, E.G., McCabe, L.J., Gerke, D.H., and Perez, J.M., "Heavy-Duty Diesel Engine/Fuels Combustion Performance and Emissions - A Cooperative Research Program," SAE Paper 852078, 1985.
16. McMillan, M., and Halsall, R., "Fuel Effects on Combustion and Emissions in a Direct Injection Diesel Engine," SAE Paper 881610, 1988.
17. Dec, J., and Coy, E., "OH Radical Imaging in a DI Diesel Engine and the Structure of the Early Diffusion Flame," SAE Paper 960831, 1996.
18. Planck, M., "Distribution of Energy in the Spectrum," *Annalen der Physik*, vol. 4, no. 3, pp. 553-563, 1901.
19. Hottel, H., and Broughton, F., "Determination of True Temperature and Total Radiation from Luminous Flame," *Industrial and Engineering Chemistry, Analytical Edition*, Vol. 4, 1932.
20. Tree, D., "Soot Particle Size and Number Density Measurements in a Direct Injection Diesel Engine using Light Scattering, Radiation, and Extinction," Ph.D. Thesis, Department of Mechanical Engineering, University of Wisconsin-Madison, 1992.

REPORT OF INVENTIONS

"Fuel Injector Nozzle with Tangential Orifices" Ali Ulidogan - Caterpillar, P.O. Box 740, Pontiac, IL 61764 and Rolf Reitz, Engine Research Center